UNIVERSITY OF WOLLONGONG AUSTRALIA

University of Wollongong - Research Online

Thesis Collection

Title: Development of new electrode materials for lithium ion batteries

Author: Chao Zhong

Year: 2010

Repository DOI:

Copyright Warning
You may print or download ONE copy of this document for the purpose of your own research or study. The University does not authorise you to copy, communicate or otherwise make available electronically to any other person any copyright material contained on this site.
You are reminded of the following: This work is copyright. Apart from any use permitted under the Copyright Act 1968, no part of this work may be reproduced by any process, nor may any other exclusive right be exercised, without the permission of the author. Copyright owners are entitled to take legal action against persons who infringe their copyright. A reproduction of material that is protected by copyright may be a copyright infringement. A court may impose penalties and award damages in relation to offences and infringements relating to copyright material.
Higher penalties may apply, and higher damages may be awarded, for offences and infringements involving the conversion of material into digital or electronic form.

Unless otherwise indicated, the views expressed in this thesis are those of the author and do not necessarily represent the views of the University of Wollongong.

Research Online is the open access repository for the University of Wollongong. For further information contact the UOW Library: research-pubs@uow.edu.au

University of Wollongong Thesis Collections

University of Wollongong Thesis Collection

University of Wollongong *Year* 2010

Development of new electrode materials for lithium ion batteries

Chao Zhong
University of Wollongong

Zhong, Chao, Development of new electrode materials for lithium ion batteries, Master of Engineering - Research thesis, Institute for Superconducting & Electronic Materials - Faculty of Engineering, University of Wollongong, 2010. http://ro.uow.edu.au/theses/3126

This paper is posted at Research Online.

NOTE

This online version of the thesis may have different page formatting and pagination from the paper copy held in the University of Wollongong Library.

UNIVERSITY OF WOLLONGONG

COPYRIGHT WARNING

You may print or download ONE copy of this document for the purpose of your own research or study. The University does not authorise you to copy, communicate or otherwise make available electronically to any other person any copyright material contained on this site. You are reminded of the following:

Copyright owners are entitled to take legal action against persons who infringe their copyright. A reproduction of material that is protected by copyright may be a copyright infringement. A court may impose penalties and award damages in relation to offences and infringements relating to copyright material. Higher penalties may apply, and higher damages may be awarded, for offences and infringements involving the conversion of material into digital or electronic form.

DEVELOPMENT OF NEW ELECTRODE MATERIALS FOR LITHIUM ION BATTERIES

A thesis submitted in fulfilment of the requirements for the award of the degree

MASTER OF ENGINEERING - RESEARCH

from

UNIVERSITY OF WOLLONGONG

by

CHAO ZHONG, B. ENG.

INSTITUTE FOR SUPERCONDUCTING & ELECTRONIC MATERIALS, FACULTY OF ENGINEERING

2010

CERTIFICATION

I, Chao Zhong, declare that this thesis, submitted in fulfillment of the requirements for the award of Master of Engineering-Research, in the Institute for Superconducting & Electronic Materials, Faculty of Engineering, University of Wollongong, is wholly my own work unless otherwise referenced or acknowledged. The document has not been submitted for qualifications at any other academic institution.

Chao Zhong

16 February 2010

For my father and mother,

who love and support me all the time

ACKNOWLEDGEMENTS

I wish to express my sincere appreciation to my research supervisor, Prof. Hua Kun Liu, and co-supervisor, Dr. Jia Zhao Wang, for their guidance, financial assistance and constant encouragement throughout my study. Many thanks also go to them for their earnest review of the manuscript. Any remaining errors are my responsibility.

I would like to express my deepest appreciation to Prof. Shi Xue Dou, Director of the Institute for Superconducting & Electronic Materials (ISEM), for introducing me to the institute and also the intriguing field of rechargeable lithium batteries, and providing me with the appropriate facilities and expertise during my study.

Technical assistance from the people in the university, such as Dr. Kosta Konstantinov (BET, TGA/DTA), Mr. Darren Attard (SEM/EDX, FE-SEM), Dr. Germanas Peleckis (XRD), Associate Professor Peter Innis (Raman spectroscopy), Dr. Zhixin Chen and Dr. David Wexler (TEM), and Mr. Ron Kinnell and Mr. Rob Morgan (technical staff) are gratefully acknowledged.

I would like to give my heartfelt thanks to Mr. Shu Lei Chou, for his kindly support and help during my Master's study. I also wish to thank Mr. Guo Dong Du, Mrs. Lin Lu, Mr. MD Mokhlesur Rahman, Mr. Peng Zhang, Mr. Qi Li, Dr. Xue Bin Zhu, Mr. Wen Xian Li, Miss Lin Wang, Mr. Yi Du, for their friendly support and kindly discussions during my study. Many thanks also go to Dr. Tania Silver for the critical reading of all my publications and proofreading of this thesis.

Finally, words can not express my gratitude for the unwavering support of my family. I wish to express my deepest respect and special thanks to my father and mother for their continue support, understanding, and love during my study to enable the completion of this thesis.

ABSTRACT

Rechargeable lithium-ion batteries that have been widely used in portable electronic devices are now extended to applications such as electric vehicles (EVs). Therefore, the performance of the rechargeable lithium-ion batteries must continue to be improved in terms of capacity, rate capability, cycle life, etc. In this Master's research study, to contribute to this goal, several materials were characterized and examined for possible applications as anode or cathode for rechargeable lithium-ion batteries. Among the anode candidates, nickel oxide (NiO), copper oxide (CuO) and copper oxide with carbon (CuO-C), and free-standing graphene-silicon (graphene-Si) were studied. Manganese dioxide (MnO_2) was also studied as a cathode material candidate for use in rechargeable lithium-ion batteries.

Hollow spherical NiO particles were prepared using the spray pyrolysis method with different concentrations of precursor for use in rechargeable lithium-ion battery anode. The electrochemical properties of the NiO electrodes, which contained a new type of binder, carboxymethyl cellulose (CMC), were examined for comparison with NiO electrodes with poly(vinylidene) fluoride (PVDF) binder. The electrochemical performance of NiO electrodes using CMC binder was significantly improved. For the cell made from 0.3 mol L^{-1} precursor, the irreversible capacity loss between the first discharge and charge was about 43% and 24% for the electrode with PVDF and CMC binder, respectively. The cell with NiO-CMC electrode has a much higher discharge capacity of 547 mAh g^{-1} compared to that of the cell with NiO-PVDF electrode, which is 157 mAh g^{-1} beyond 40 cycles.

Bare copper oxide and copper oxide–carbon composite were synthesized by a one-step spray pyrolysis method and tested as anode materials combined with CMC or PVDF binder for rechargeable lithium-ion batteries. The results demonstrate that the CuO-carbon composite in conjunction with CMC binder has excellent electrochemical performance, with a capacity of 633 mAh g^{-1} up to 250 cycles at a current density of 100 mA g^{-1}. Usage of the water soluble binder, CMC, not only further confirmed its potential for improving the electrochemical performance of transition metal oxides for use in lithium-ion batteries, but also makes the electrode fabrication process much easier and more environmentally friendly.

Flexible, free-standing, paper-like, graphene-silicon composite materials have been synthesised by a simple, one-step, in-situ filtration method. The Si nanoparticles are highly encapsulated in a graphene nanosheet matrix. The electrochemical results show that graphene-Si composite film has much higher discharge capacity beyond 100 cycles (708 mAh g^{-1}) than that of the cell with pure graphene (304 mAh g^{-1}). The graphene functions as a flexible mechanical support for strain release, offering an efficient electrically conducting channel, while the nanosized silicon provides the high capacity.

Finally, nanocrystalline MnO_2 powders were synthesized by a novel magnetic field assisted hydrothermal method and tested as cathode material in rechargeable lithium-ion batteries. It was found that the morphology of the MnO_2 prepared without magnetic field is characterized by an urchin-like structure, while the MnO_2 prepared in magnetic fields has a rambutan-like structure. A pronounced increase in the

Brunauer-Emmett-Teller (BET) specific surface area was obtained when the intensity of the pulsed magnetic field increased. The battery performance was improved for the samples prepared with magnetic fields. The MnO_2 prepared under a magnetic field of 4 T shows a capacity of 121.8 mAh g^{-1} after 30 cycles, while the MnO_2 prepared without magnetic field only shows 103.0 mAh g^{-1} after 30 cycles.

TABLE OF CONTENTS

LIST OF FIGURES

LIST OF TABLES

CHAPTER 1 INTRODUCTION

Energy production and consumption that rely on the combustion of fossil fuels have had severe impacts on world economics and ecology [1]. Electrochemical energy conversion and storage systems, which include batteries, fuel cells, and supercapacitors, are undoubtedly playing a very important role as an alternative because the energy consumption is designed to be more sustainable and more environmentally friendly. The rechargeable lithium-ion battery is one of the most promising candidates because it offers several advantages compared to the others, such as its higher energy density (up to 180 Wh kg^{-1}), higher cell voltage (up to about 3.8 V per cell), and longer charge retention or shelf life (up to 5-10 years). The lithium-ion battery market has grown in decades from a research & development interest to sales of over 1.1 billion units with value of over $4 billion by 2005, as described by David Linden et al [2].

In the study of rechargeable lithium-ion batteries, there are several main areas of research, such as anode materials, cathode materials, electrolytes, binders, separators and the overall construction or design of the cell. This study mainly focuses on developing new electrode materials with the proper binder to achieve better electrochemical properties for use in rechargeable lithium-ion batteries.

Chapter 2 of the present study commences with a literature review related to rechargeable lithium-ion batteries. The chapter includes an overview of the general background, a brief history, basic concepts and principles, and general components

of rechargeable lithium-ion batteries, followed by the recent research and development in this area.

Chapter 3 presents the overall experimental methods and procedures used in this study, and the starting materials and chemicals used in the synthesis and fabrication. Additional specific details are given at the beginning of each chapter as required.

Chapter 4 presents a synthesis and characterization study of nanocrystalline nickel oxide hollow sphere materials prepared by a simple one-step spray pyrolysis method for rechargeable lithium-ion battery anode. The as-prepared materials were investigated by X-ray diffraction (XRD), scanning electron microscopy (SEM), and transmission electron microscopy (TEM). A new type of binder, carboxymethyl cellulose (CMC), was tested to combine with the as-obtained material for comparison with the conventional poly(vinylidene) fluoride (PVDF) binder. Coin-type cells were constructed using the as-synthesized powders as the active material, and the electrochemical performance of these cells was assessed by using galvanostatic charge and discharge cycling, as well as electrochemical impedance spectroscopy (EIS).

Chapter 5 continues with carbon coating as an approach to improve the electrochemical properties of the transition metal oxide used in rechargeable lithium-ion battery anode. In this chapter, copper oxide-carbon composite was prepared using a simple one-step spray pyrolysis method. XRD was used to determine the structural parameters. The morphologies of the powders were investigated by SEM, field emission SEM (FE-SEM) and TEM. Energy dispersive X-ray (EDX) mapping and

thermogravimetric analysis (TGA) were performed to examine the carbon content. The positive potential of using CMC as the binder for transition metal oxides for rechargeable lithium-ion batteries was also confirmed in this study.

Chapter 6 explores a new free-standing anode material, graphene-silicon composite film, which was synthesized by a simple filtration technique. Different physical and electrochemical characterization methods, including XRD, Raman, FE-SEM, EDX mapping, TGA, and charge-discharge testing were used to study the as-obtained composite film-like material.

Chapter 7 is a preliminary study on the synthesis and characterization of manganese dioxide as cathode material for rechargeable lithium batteries using a novel magnetic field assisted hydrothermal method. Different methods including XRD, FE-SEM, TEM, the Brunauer-Emmett-Teller (BET) technique, cyclic voltammetry (CV), and charge-discharge testing were used to study the as-prepared materials physically and electrochemically.

General conclusions for these studies are given in Chapter 8.

CHAPTER 2 LITERATURE REVIEW

2. 1 Introduction to Rechargeable Lithium-ion Batteries

2.1.1 General Introduction

Lithium is the lightest metallic element with atomic weight 6.94 amu, and it has the smallest electrochemical equivalent weight at 3.86 Ah g^{-1}, as well as the lowest standard electrode potential at -3.05 V. All of these characteristics make lithium an electrode material with high specific energy. The development of lithium-ion batteries has resulted from the use of lithium anode material, and the safety problems in the application of lithium batteries promoted the great development of lithium-ion secondary batteries.

In February 1990, Sony first announced that they had invented a practical Rocking-Chair battery using $LiCoO_2$ as cathode material and refinery coke as anode. This battery had good performance in charge and discharge and had a high capacity. They proposed the "Lithium-ion Battery" for the first time in the world. The greatest success of this system was in using carbon material which can allow Li ions to insert and de-insert themselves reversibly, instead of using Li metal as anode. Over the past 20 years, lithium-ion battery technology has been constantly improved and is fast becoming the first choice of power sources for hand-held video cameras, mobile phones, laptops, portable power tools, and other electronic products. Large-scale lithium-ion batteries are prime contenders as power sources for electric vehicles (EVs) and for load-levelling applications. Figure 2.1 compares the energy densities

of the different types of rechargeable batteries [3]. It is obvious that lithium-ion batteries deliver the highest energy density among the different systems.

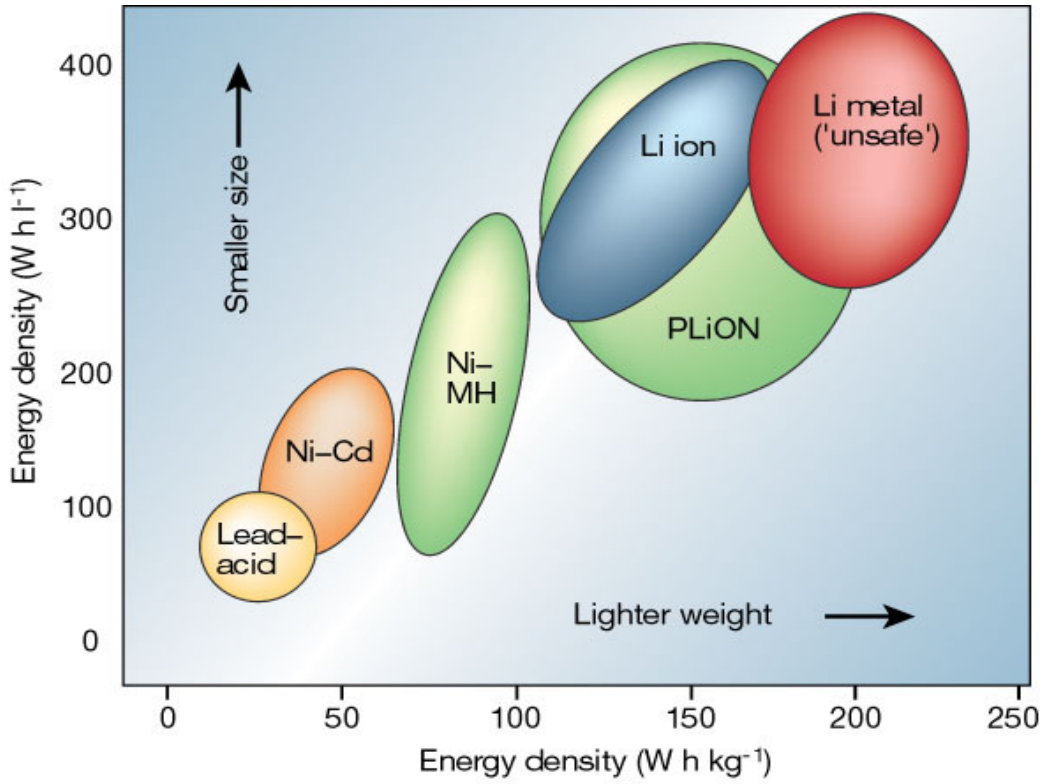

Figure 2.1 Energy densities of the different types of rechargeable batteries [3].

The major advantages and disadvantages of lithium-ion batteries, relative to other types of batteries, are summarized in Table 2.1 [2].

Table 2.1 Advantages and disadvantages of lithium-ion batteries [2].

Advantages	***Disadvantages***
Sealed cells; no maintenance required;	Moderate initial cost;
Long cycle life;	Degrades at high temperature;

Broad temperature range of operation;	Need for protective circuitry;
Long shelf life;	Capacity loss or thermal runaway when over-charged;
Low self-discharge rate;	Venting and possible thermal runaway when crushed;
Rapid charge capability;	Cylindrical designs typically offer lower power density than NiCd or NiMH.
High rate and high power discharge capability;	
High coulombic and energy efficiency;	
High specific energy and energy density;	
No memory effect.	

2.1.2 A Brief History

The development of modern batteries as a form of energy storage can be traced to Galvani in the 1790s [4]. Interest increased in this new area rapidly, and in 1800, Volta outlined his design of a device that could produce a constant current from the proper assembly of dissimilar metals which became known as the “voltaic pile” [5]. In 1802, Cruickshank replaced silver with copper and inserted the cell into a brine filled box, which enabled the cells to be mass produced [6]. Serious development of battery systems with high-energy-density was commenced in the 1960s and concentrated on nonaqueous primary batteries using lithium as the anode material. The first lithium-based battery which was a non-rechargeable type was demonstrated in the early 1970s in selected military applications. However, during that time, use was limited as suitable cell structures, formulations, and safety issues needed to be resolved. The commercialization of rechargeable lithium-ion batteries was first achieved in 1991 by the Sony Company in Japan. The history of battery development is listed as follows in Table 2.2.

Table 2.2 History of battery development.

1600	***Gilbert (UK)***	***Establishment of electrochemistry study***
1791	Galvani (Italy)	Discovery of "animal electricity"
1800	Volta (Italy)	Invention of the voltaic cell
1802	Cruickshank (UK)	First electric battery capable of mass production
1820	Ampere (France)	Electricity through magnetism
1833	Faraday (UK)	Announcement of Faraday's Law
1836	Daniell (UK)	Invention of the Daniell cell
1839	Grove (UK)	Invention of the fuel cell (H_2/O_2)
1859	Plante (France)	Invention of the lead acid battery
1868	Leclanche (France)	Invention of the Leclanche cell
1888	Gassner (USA)	Completion of the dry cell
1899	Jungner (Sweden)	Invention of the nickel-cadmium battery
1901	Edison (USA)	Invention of the nickel-iron battery
1932	Shlecht &Ackermann (Germany)	Invention of the sintered pole plate
1947	Neumann (France)	Successfully sealing the nickel-cadmium battery
1960	Union Carbide (USA)	Development of primary alkaline battery
1970		Development of valve regulated lead acid battery
1990		Commercialization of nickel-metal hydride battery
1991	Sony (Japan)	Commercialization of lithium-ion battery

2.1.3 Basic Principles of Lithium-ion Batteries

Electrochemistry covers all reactions in which a chemical change is the result of electric forces and, in the reverse case, where an electric force is generated by a chemical process [2].

A galvanic cell is an electrochemical cell that generates electricity as result of the spontaneous reaction occurring inside it. The cell consists of two dissimilar electrodes (the anode and the cathode) immersed in an electrolyte solution. The electrodes are electronic conductors, and the electrolyte solution is an ionic

conductor. At the interface between the electronic and the ionic conductors, the passage of electrical charge is coupled with a chemical traction. This type of action is known as a redox reaction, where there is a transfer of electrons from one species to another. There are two half reactions, which involve at the anode the oxidation (Ox) of one species (the removal of electrons) and at the cathode the reduction (Red) of another (the addition of electrons).

At the anode: $Red1 \rightarrow Ox1 + e^-$ (2.1)

At the cathode: $Ox2 + e^- \rightarrow Red2$ (2.2)

Overall reaction: $Red1 + Ox2 \rightarrow Ox1 + Red2$ (2.3)

A battery consists of one or more electrochemical units which we called “cells”. These cells are connected in series or parallel, or both, depending on the designed output voltage and capacity. Generally, a typical cell consists of four major components, as shown in Figure 2.2 [3]. They are an anode, a cathode, a separator, and the electrolyte among them.

(a) The anode, or negative electrode, or the reducing electrode, gives up electrons to the external circuit and is oxidized during the electrochemical reaction.

(b) The cathode, or positive electrode, or the oxidizing electrode, accepts electrons from the external circuit and is reduced during electrochemical reaction.

(c) The electrolyte or the ionic conductor provides the medium for transfer of electrons, as ions, inside the cell between the anode and cathode. The electrolyte is typically a liquid (an organic solvent, such as ethylene carbonate (EC)-dimethyl carbonate (DMC)), with dissolved salts (such as $LiPF_6$) to impart ionic

conductivity. Some batteries use solid electrolytes, which are ionic conductors at the operating temperature of the cell.

(d) The separator mainly has two functions. One is to keep the cathode and anode electrodes apart, and the other is to serve as a safety device. When a cell becomes too hot, the low-melting point polymers melt, thereby shutting off the cell current.

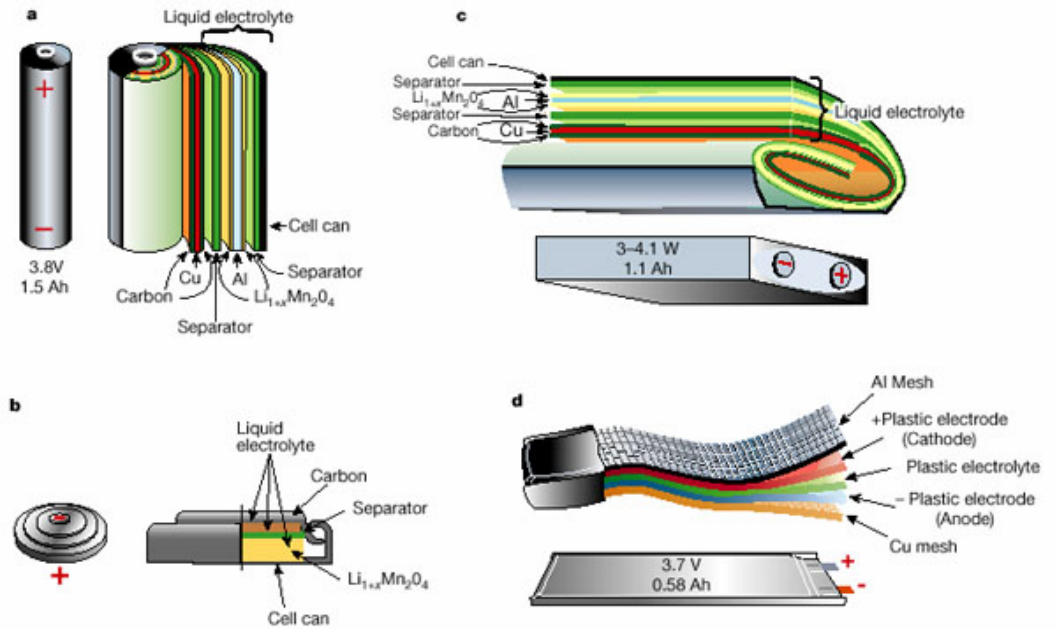

Figure 2.2 Schematic drawing showing the shape and components of various Li-ion battery configurations: a, Cylindrical; b, coin; c, prismatic; and d, thin and flat [3].

Figure 2.3 shows the theoretical specific capacities of different electrode materials [3]. For the anode (negative) materials, the lower the potential (vs. Li/Li^+) the better, and the opposite is true for cathode (positive) materials. It is obvious that there are huge differences in capacity between Li metal and the other anode electrodes, while the safety problem caused by dendrite growth is serious. Another issue is that although the capacities of anode materials are generally much higher than those of

cathode materials, the real specific capacities of anodes in commercial use are lower due to a number of reasons (tap density, substrate, etc). So research and development (R&D) on both anode and cathode materials are equally important.

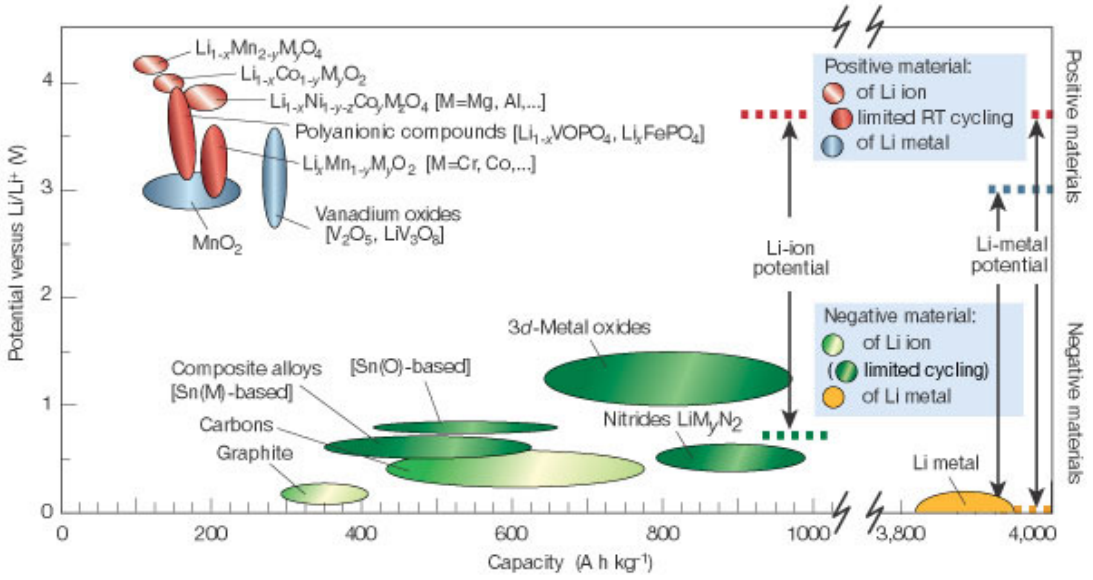

Figure 2.3 Voltage versus capacity for positive and negative electrode materials [3].

2. 2 Anode Electrode Materials

Because of the high specific capacity of the lithium metal, it was always seen as the first choice of anode material in lithium batteries during the 1970s and early 1980s. However, lithium batteries were unsuccessful in the early period. The main reason was the safety problem caused by using a lithium metal anode. During the charge and discharge cycle, lithium is often deposited in dendrites. The dendrites gradually grow during the cycle and penetrate the separator after a certain number of cycles, which could lead to short circuiting. Due to these safety problems, researchers turned to

alternative anode materials. The successful commercial application of lithium-ion batteries is mainly attributable to the use of lithium compounds instead of Li metal as the anode. Ideal anode materials should have the following conditions:

(a) Good reversibility and charge-discharge cycle life;
(b) High specific capacity;
(c) Good compatibility with electrolyte solution;
(d) Low first irreversible capacity;
(e) Safety, environmentally friendliness;
(f) Abundant raw materials, simple synthesis process, inexpensive.

However, the existing anode materials can not meet all the above requirements at the same time. Therefore, research and development of a new anode material with better electrochemical characteristics has become a hot topic in the lithium-ion batteries research field. Graphitic carbon is currently the most often employed material for the negative electrode due to its low cost, excellent cycling stability and reliability, and non-toxicity [3, 7, 8]. Table 2.3 is a list of alternative anode materials for Li-ion batteries [9].

2.2.1 Carbonaceous Materials

A very important reason for the rapid commercialization of lithium-ion batteries is the application of carbonaceous-based materials. This has been mainly due to the following reasons:

(a) Low cost;

(b) High safety for people and the environment;

(c) Low Li-ion insertion potential (~0.1V vs. Li/Li^+), which is very close to that for metallic lithium;

(d) Good cycling stability due to the high mechanical integrity (compared to metal alloys) of the electrode even after 500 charge-discharge cycles; and

(e) Higher specific charge compared to transition metal oxides or transition metal sulphides (see Table 2.3).

Table 2.3 List of alternative anode materials for lithium-ion batteries [9].

	Negative Electrode Material (Reduced phase in brackets)	**Molar mass/ g mol^{-1}** (Related to lithium-free material)	**Theoretical specific charge capacity/ Ah kg^{-1}** (Related to lithium-free material)	**Potential of reaction/ V vs. Li/Li$^+$**
	Li metal	6.94	3862	0
Carbon	Graphite (LiC_6)	72.06	372	0.1
Carbon	Hard carbons (LiC_x)	-	400-2000	0 - 1.1 V
Metal alloys (binary and ternary)	Al (LiAl)	26.98	993	0.35
Metal alloys (binary and ternary)	Sn ($Li_{21}Sn_5$)	593.55	948	0.42 - 0.66
Metal alloys (binary and ternary)	Sb (Li_3Sb)	121.75	660	0.9
Metal alloys (binary and ternary)	Si ($Li_{4.2}Si$)	28.09	4200	0.5
Metal alloys (binary and ternary)	Cu_6Sn_5 ($Li_{22}Sn_5$ + 6Cu)	974.73	605	0.1
Layered TM Oxides	WO_2 ($LiWO_2$)	215.85	124	0.3 - 1.4
Layered TM Oxides	MoO_2 ($LiMoO_2$)	127.94	209	0.8 – 2.0
Layered TM Oxides	MoS_2 ($LiMoO_2$)	160	168	1.3 – 2.3
Layered TM Oxides	TiS_2 ($LiTiS_2$)	112.01	239	1.5 – 2.7
Spinel	$Li_4Ti_5O_{12}$ ($Li_7Ti_5O_{12}$)	459.26	175	1.56
Anatase	TiO_2 ($Li_{0.5}TiO_2$)	80	168	1.78

The insertion of lithium into carbon is referred to as intercalation, with intercalation being formally described as the insertion of a guest species into a layered host structure, without any major resulting structural changes [8]. In half-cell reactions

against metallic lithium, lithium-ion intercalation into carbon is referred to as the discharge step, while the de-intercalation process is the charge step.

$$C_n + xLi^+ + xe^- \leftrightarrow Li_xC_n \tag{2.4}$$

Carbon is the most widespread element in the nature. Because of the sources and methods of preparation, it has a large variety of complex structures. We can now prepare many types of carbon materials in industry which have a tremendous impact on the electrochemical properties (lithium-ion insertion capacity and potential). At present, there are mainly three types of carbon used in lithium-ion batteries: they are soft carbon, hard carbon, and graphite (Figure 2.4).

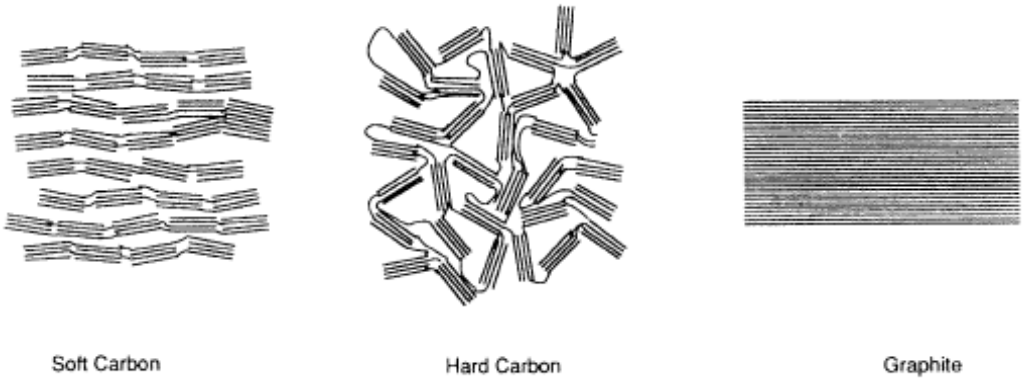

Figure 2.4 The structures of three different types of carbonaceous materials.

In 1990, coke was used by Sony as anode to solve the propylene carbonate co-intercalation problem [10]. Later, graphitized mesophase microbeads (MCMBs) became more popular [11, 12]. MCMB carbons offer good capacity, ~300 mAh g^{-1}, and low irreversible capacity, ~20 mAh g^{-1}. Lower cost graphite offers a higher theoretical capacity of 372 mAh g^{-1} to form LiC_6, but has a higher irreversible

capacity of ~50 mAh g^{-1} and higher fade rates than MCMB carbons. Since 1990, many efforts have been made to develop high capacity anode materials to replace graphite. Non-graphitized carbon materials, including soft carbon and hard carbon, have been widely studied [13, 14, 15].

More recently, graphene, a single layer of carbon (carbon atoms in a two-dimensional honeycomb lattice), was found to exist in a free-standing form and exhibits many unusual and intriguing physical, chemical, and mechanical properties [16, 17]. Due to the high quality of the sp^2 carbon lattice, electrons were found to move ballistically in graphene layers even at ambient temperature [18, 19]. One of most exciting possibilities is the use of bulk graphene powders as anode materials for reversible lithium storage in lithium-ion batteries [20, 21]. In this research study, graphene powder was synthesized and used as both an active material and a conductive additive to form a free-standing silicon-graphene film using a filtration technique. In the related chapter, exploration of using this material as an anode material for rechargeable lithium-ion batteries is discussed.

2.2.2 Lithium-metal Alloys

The electrochemical alloying reaction of lithium with metals has been widely studied since the 1970s [8, 22, 23]. Lithium can form intermetallic compounds with many other metals and store a large quantity of lithium by the formation of alloys ($Li_{4.4}Si$, which corresponds to a Li storage capacity of 4200 mAh g^{-1}, $Li_{4.4}Ge$: 1600 mAh g^{-1}, LiAl and $Li_{4.4}Sn$: 990 mAh g^{-1}, and Li_3Sb: 665 mAh g^{-1}). The electrochemical charge/discharge processes of these alloys are apparently very simple, since they are based on the lithium alloying in charge and de-alloying in discharge:

$$M + xLi \leftrightarrow Li_xM \quad (2.5)$$

However, in practice, the use of these Li-M alloys as electrodes in a lithium cell is affected by the large volume expansion/shrinkage that they experience in the course of the electrochemical processes of lithium alloying/de-alloying, i.e. with a volume change of the order of 310, 255 and 130%, associated with the lithium alloying with Si, Sn, and Sb, respectively [24]. Then, volume stresses lead over the course of a few cycles to cracks and pulverisation, and thus, to a fast electrode decay [25]. Some works have shown that synthesis of nanosized alloys could improve the cyclic performance [26, 27]. The recently commercialized Sony Nexelion cell used a tin-based amorphous alloy anode [28]. Although tin experiences a large volume change on Li insertion, the tin-based amorphous alloy obtained by Sony was shown to exhibit 92% capacity retention after 100 cycles.

In one chapter of this thesis, nanosilicon powder was selected as the subject because it has the highest theoretical capacity. The fabrication of nanosilicon-graphene composite film was mainly designed to solve the big volume change problem of silicon material during charge and discharge cycles.

2.2.3 Transition Metal Oxides

Transition metal oxides were long regarded as only cathode materials. This situation was not changed until it was demonstrated that lithium ions could intercalate and de-intercalate into/from their crystal structure reversibly at low potential [29]. Transition metal oxides can be divided into two categories according to the different

mechanisms of lithium intercalation and de-intercalation. One class is oxides such as TiO_2, MoO_2, Nb_2O_5, etc., which can be reversibly inserted with lithium ions, without formation of Li_2O. The other is represented by MO (M = Co, Ni, Cu, Fe), in which the insertion of lithium ions is accompanied by the formation of Li_2O. The reaction process involves the formation and decomposition of Li_2O, accompanying the reduction and oxidation of the metal particles via the following displacement reaction [29]:

$$M_xO_y + 2yLi \leftrightarrow xM + yLi_2O \quad (2.6)$$

It had long been reported that bulk Li_2O was electrochemically inactive and therefore unable to be decomposed. However, by manufacturing nanostructured MO precursors, the resultant Li_2O is also nanostructured and may be decomposed [29, 30]. This finding made it possible that the reaction of nanostructured MOs with lithium can be completely reversible, and these materials received significant attention as possible anode materials for use in lithium-ion batteries [31]. Previous reports showed that MO nanoparticles can exhibit reversible capacities up to 700 mAh g^{-1} [32, 33, 34, 35], and this capacity is almost three times larger than that of the graphite based anode electrodes that are currently used in commercial rechargeable lithium-ion batteries.

In this research study, two transition metal oxides, nickel oxide and copper oxide, were synthesized via a simple one-step spray pyrolysis method. Particle size was controlled by changing the concentration of the precursor solutions. The spray pyrolysis method was also considered as a new prospect for the carbon-coating work

in this study. Carbon-coated copper oxide material was designed and synthesized to overcome the drawbacks of low conductivity and big volume change during charge and discharge.

2. 3 Cathode Electrode Materials

The usual lithium-ion batteries use lithium-based metal oxides as cathode materials. The first commercialized cathode material for lithium-ion batteries was $LiCoO_2$ from Sony. In recent years, researchers developed more low-cost materials such as $LiMn_2O_4$ (spinel) and $LiFePO_4$, and some others with higher capacity such as $LiNi_{1-x}Co_xO_2$.

The key requirements for a material to be used as a cathode in a rechargeable lithium battery are [36]:

(a) The material contains a readily reducible/oxidizable ion, for example transition metals.
(b) The material reacts reversibly with lithium via an intercalation-type reaction in which the host structure essentially does not change as lithium is added.
(c) The material reacts with lithium with a high free energy of reaction: high capacity, one lithium ion per transition metal ion at least; high voltage, preferably around 4 V.
(d) The material reacts with lithium rapidly both on intercalation and de-intercalation.
(e) The material should have good electronic conductivity.

(f) The material should be stable, for example it does not change structure or otherwise degrade, when being over-discharged and over-charged.

(g) Ease and low cost of synthesis.

(h) The material should be environmentally benign.

At present, almost all the cathode materials that are being investigated and commercialized can be divided into two classes. The first class consists of layered compounds with an anion close-packed or almost close-packed lattice in which alternate layers between the anion sheets are occupied by a redox-active transition metal. Lithium then inserts itself into the essentially empty remaining layers.

This kind of structure is shown in Figure 2.5 [36]. The materials in the other class have more open structures, such as many of the vanadium oxides and transition-metal phosphates (e.g. $LiFePO_4$).

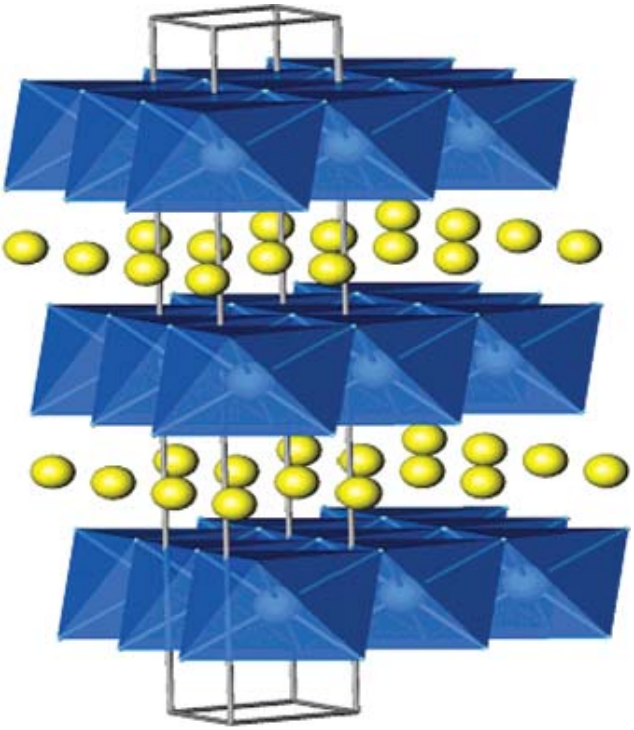

Figure 2.5 Schematic drawing of layered structure (e.g. $LiTiS_2$, $LiCoO_2$ and $LiNiO_2$) which shows the lithium ions between the transition-metal oxide/sulfide sheets [36].

2.3.1 Nanostructured Lithium Transition Metal Oxides

At present, there are three intercalation materials that have been used commercially as cathode materials for rechargeable lithium-ion batteries. They are $LiCoO_2$, $LiNiO_2$, and $LiMn_2O_4$.

The good cyclability and stability of $LiCoO_2$ has allowed it to become the most widely used cathode material in commercial lithium-ion batteries [2, 3, 8, 36]. The Sony Company combined the $LiCoO_2$ cathode with a carbon anode to make the first successful lithium-ion battery [37, 38], which now dominates the lithium battery market. The operating voltage of $LiCoO_2$ is 3.9 V, and it has a theoretical capacity of about 274 mAh g^{-1}. Actually, at most, only about half of the lithium can be reversibly extracted and inserted due to structural restriction. So good electrochemical performance can be obtained up to 4.2 - 4.25 V versus Li/Li^+, providing about 150 mAh g^{-1} capacity, and the battery may be reversibly cycled over 1000 charge-discharge cycles without appreciable specific capacity loss.

Another layered compound, $LiNiO_2$, which is isostructural with lithium cobalt oxide, has a higher theoretical and practical capacity, which is 274 and 140 - 170 mAh g^{-1}, respectively, but it has not been pursued in the pure state as a battery cathode for a variety of reasons, even though nickel is more readily available than cobalt. Firstly, it is not very clear that stoichiometric $LiNiO_2$ exists. The Li-Ni-O system is always represented by $Li_{1-y}Ni_{1+y}O_2$ with a deviation from the normal stoichiometry [39, 40].

So this special structure makes it very difficult to synthesize the stoichiometric oxide with all the lithium sites completely filled by lithium. Secondly, it suffers from poor thermal stability in its highly oxidized state (Ni^{3+}/Ni^{4+}), so that such cells are inherently unstable and therefore dangerous in contact with organic solvents.

The spinel $LiMn_2O_4$ is the third-most-popular cathode material for lithium-ion batteries. In comparison with $LiCoO_2$ and $LiNiO_2$, $LiMn_2O_4$ has been received much interest because it provides the essential advantages of low toxicity and of having abundant raw materials sources [41, 42, 43]. In principle, $Li_xMn_2O_4$ permits the intercalation/ extraction of lithium ions in the range of $0 < x < 2$. For intermediate values of x between 1 and 2, the material consists of two different phases: cubic in bulk and tetragonal at the surface. The intercalation of lithium ions leads simultaneously to a pronounced cooperative Jahn-Teller effect, in which the cubic spinel crystal becomes distorted tetragonal with $c/a \approx 1.16$, and the volume of the unit cell increases by 6.5%. Such distortion accompanying the volume change in the unit cell would cause the crystal structure of the electrode to degrade and the electrochemical properties to deteriorate. The electrochemical properties of $LiMn_2O_4$ spinel such as capacity and rechargeability vary greatly with different synthesis routes. The low temperature synthesized $LiMn_2O_4$ spinels have a high capacity, but poor cycle life.

2.3.2 Olivine

Research interests were greatly changed in 1997 with the discovery of the electrochemical properties of the olivine phase, in particular lithium iron phosphate ($LiFePO_4$) [44]. Presently, it is at the centre of much interest as cathode for lithium-

ion batteries as this is the first cathode material with potentially low cost and plentiful elements that is also environmentally benign. The olivine structure is shown in Figure 2.6. It can be used at 90% of its theoretical charge capacity (165 mAh g^{-1}) at a steady voltage of around 3.4 V by reducing the particle size (<1 μm) and when carbon was intimately mixed with the cathode material, capacities close to 100% of the theoretical capacity at rates up to 5 C were achieved [45, 46, 47, 48, 49].

The conductivity of the pure $LiFePO_4$ is only 10^{-9} S cm^{-1} as reported [48]. Therefore, many efforts have been made on improving this weakness. Results on undoped and doped $Li_{1-x}M_xFePO_4$ (M = Mg, Al, Ti, Nb or W) synthesized by solid-state reaction [48], nanosized $LiFePO_4$ powder synthesized by heating amorphous $LiFePO_4$ [50], and carbonaceous coatings deposited on the surface of $LiFePO_4$ [51] are results on the methods usually employed to solve the conductivity issue.

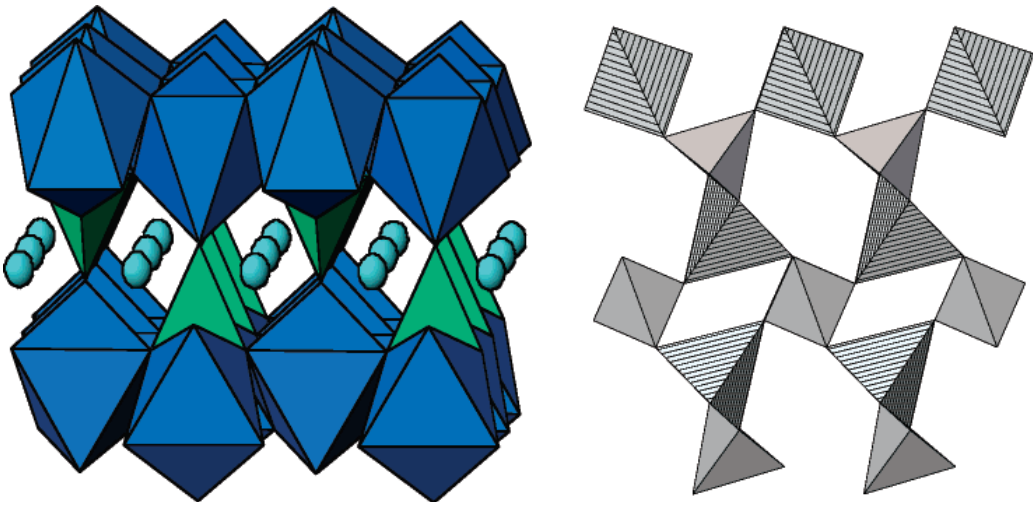

Figure 2.6 Structures of orthorhombic $LiFePO_4$ and trigonal quartz-like $FePO_4$.

2.3.3 Other Oxide Materials

Vanadium oxide is another attractive intercalation composite as a result of its layered structure. The reversible electrochemical lithium intercalation into V_2O_5 at room temperature was first reported by Whittingham in 1975 [52]. For lithium-ion intercalation applications, vanadium oxide offers the essential advantages of low cost, abundant raw materials, easy synthesis, and high energy densities. However, the average discharge voltage is around 2.5 V and is not as high as those of other compounds such as $LiCoO_2$. Crystalline V_2O_5 with a shear structure [53, 54], amorphous α-V_2O_5 [55], α-V_2O_5-B_2O_3, and α-V_2MoO_8 [56] have all been considered. However, limited cycling stability remains a big problem of such electrode materials.

In this study, manganese dioxide was synthesized using a novel magnetic field assisted hydrothermal method and tested as a cathode material in rechargeable lithium batteries. Different morphologies were obtained by changing the intensity of the magnetic field. The material synthesized under a 4 T magnetic field had the largest specific surface area and presented the best electrochemical properties.

2. 4 Electrolytes for Lithium-ion Batteries

The electrolyte is another very important factor for lithium-ion batteries because the electrochemical performance is strongly dependent on it. Four types of electrolytes have been used in lithium-ion batteries: liquid electrolytes, gel electrolytes, polymer electrolytes, and ceramic electrolytes. Liquid electrolytes are solutions of a lithium

salt in organic solvents, typically carbonates. A polymer electrolyte is a liquid- and solvent-free material, where an ionically conducting phase is formed by dissolving a salt in a high molecular weight polymer, whereas a gel electrolyte is an ionically conductive material in which a salt and a solvent are dissolved or mixed with a high molecular weight polymer. Ceramic electrolytes refer to inorganic, solid-state materials that are ionically conductive [2].

Most lithium-ion electrolytes in current use utilize $LiPF_6$ as the salt, as its solutions offer high ionic conductivity, $> 10^{-3}$ S cm^{-1}, high lithium ion transference number (~0.35), and acceptable safety properties. The carbonate solvents currently used are ethylene carbonate (EC), dimethyl carbonate (DMC), ethyl methyl carbonate (EMC) and diethyl carbonate (DEC).

2. 5 Binders for Lithium-ion Batteries

In order to enhance the performance of lithium-ion batteries, researchers and battery manufacturers are not only trying to create new electrode materials, but also searching for new binders, since battery efficiency is strongly dependent on the electrode engineering [57, 58, 59]. The binder has to survive the large repeated dimensional changes of the electrode during the cycling of the cell. In commercial lithium-ion batteries, poly(vinylidene) fluoride (PVDF) has been used as binder for both the anode and the cathode electrodes because of its good electrochemical stability and high adhesion to the electrode materials and current collectors.

However, using PVDF has the following drawbacks:

(a) PVDF is only soluble in organic solvents, and it is expensive and dangerous to humans and the environment;

(b) Control of the humidity (less than 2%) is needed during the electrode preparation.

Recent studies have shown that the choice of a new binder is very important to stabilize the cycling performance [57, 59]. Li et al. reported that Fe_2O_3 electrodes using carboxymethyl cellulose (CMC) binder show better cycling performance (about 800 mAh g^{-1} for 100 cycles) compared to electrodes made from conventional PVDF binder [60]. Chou et al. also reported that SnO_2 electrode with CMC binder gave better performance than with PVDF [61]. Besides, the CMC has other obvious advantages:

(a) Low cost,

(b) No pollution problems, and

(c) No requirement for strict control of the processing humidity, which is of great importance for battery production.

In this study, electrode materials were tested combined with CMC and PVDF binders to explore the effect of different binders in lithium-ion batteries.

CHAPTER 3 EXPERIMENTAL

3. 1 List of materials

The list of materials and chemicals used during my Master's studies for the synthesis and characterization of materials is summarized in Table 3.1.

Table 3.1 Description of chemicals used during my Master's studies.

Materials/Chemicals	Formula	Purity (%)	Supplier
Nickel nitrate hexahydrate	$Ni(NO_3)_2 \cdot 6H_2O$	≥98.5	Aldrich
Copper(II) nitrate trihydrate	$Cu(NO_3)_2 \cdot 3H_2O$	99.5	BDH
Sucrose	$C_{12}H_{22}O_{11}$	98	Aldrich
Graphite	C	-	Fluka
Sulfuric acid	H_2SO_4	95-98	Sigma-Aldrich
Potassium peroxodisulfate	$K_2S_2O_8$	≥99	Sigma-Aldrich
Phosphorus pentoxide	P_2O_5	≥98	Sigma
Potassium permanganate	$KMnO_4$	≥99	Sigma-Aldrich
Hydrochloric acid	HCl	37	Sigma-Aldrich
Sodium hydroxide	NaOH	≥98	Sigma-Aldrich
Pyrenebutyric acid	$C_{20}H_{16}O_2$	97	Aldrich
Hydrazine monohydrate	$N_2H_4 \cdot H_2O$	98	Sigma-Aldrich
Silicon	Si	-	China
Triton X-100	$(C_2H_4O)_n \cdot C_{14}H_{22}O$	-	China
Manganese sulfate monohydrate	$MnSO_4 \cdot H_2O$	99	China
Ammonium persulfate	$(NH_4)_2S_2O_8$	≥98.5	China
1-methyl-2-pyrrolidinone	C_5H_9NO	99.5	Sigma-Aldrich

Poly(vinylidene) fluoride (PVDF)	$(CH_2CF_2)_n$	-	Sigma-Aldrich
Carboxymethyl cellulose (CMC)	-	-	Sigma
Lithium metal	Li	-	China
Copper foil	Cu	-	China
Aluminium foil	Al	-	China
Carbon black	C	-	Timcal, Belgium
Electrolyte	1.0 M $LiPF_6$ in 1:1 EC/DMC		China

3. 2 Experimental procedure

3.2.1 Overall Framework of the Experiments

Figure 3.1 shows the overall framework of the experiments I conducted in this research work.

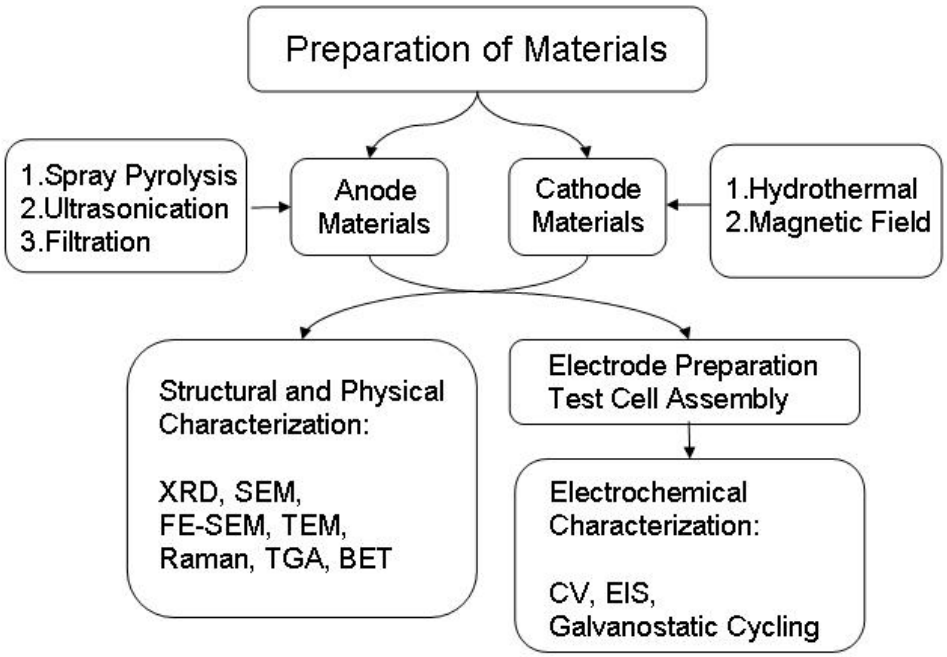

Figure 3.1 The overall framework of the experiments.

3.2.2 Materials Preparation

(a) Spray Pyrolysis

The spray pyrolysis method was used to synthesize spherical NiO, CuO, and CuO-carbon composite anode materials in this research work. The experimental set-up is schematically depicted in Figure 3.2 [62]. The facility mainly comprised a peristaltic pump that feeds the liquid at the set flow rate, an atomizing nozzle in combination with compressed air, a tubular furnace, and an extractor pump. In a typical experiment in this work, the solution was peristaltically pumped into a three-zone spray pyrolysis furnace at a set operating temperature, using compressed air as the carrier gas. The resultant powder was separated from the hot gas stream via a collecting jar and collected into airtight sample bottles.

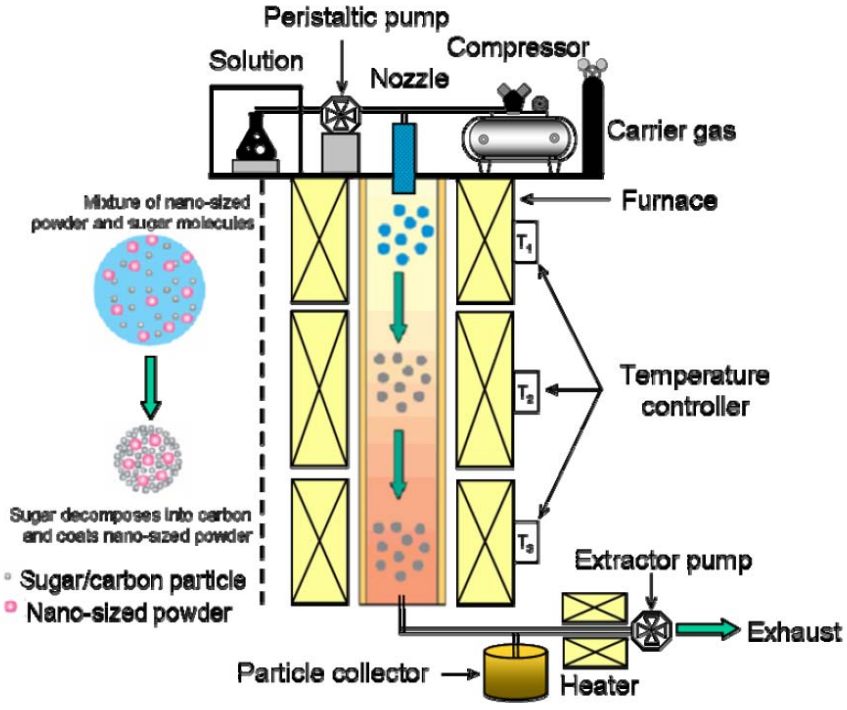

Figure 3.2 Schematic diagram of spray pyrolysis apparatus.

(b) Ultrasonication

In the experiments, ultrasonication was used to improve the mixing and chemical reactions. The parameters of the ultrasonicator (SONICS hand held welder) were adjusted as follows: power output < 18 W, 3 seconds on/off for 3 hours.

(c) Filtration Technique

In this work, a filtration technique was used to fabricate silicon-graphene composite films. Firstly, a dispersion of silicon-graphene/Triton X-100 in de-ionized water was prepared. Secondly, a poly(vinylidene) fluoride (PVDF) membrane (pore size 0.22 μm GV Millipore) was wetted in a 50:50 v/v de-ionized water to ethanol solution for 30 minutes. Then, passing the as-prepared suspension through the wetted PVDF filter in a filtration cell (Whatman 47 mm, as shown in Figure 3.3) under a positive pressure of 400 kPa produced a "free-standing" mat of silicon-graphene. Subsequently, the resultant film was washed with 200 ml of de-ionized water. Finally, the film was peeled off from the PVDF filter after drying overnight in a vacuum oven.

Figure 3.3 Filtration process using Whatman 47 mm filtration cell.

(d) Magnetic Field Assisted Hydrothermal Method

A magnetic field assisted hydrothermal method was used in this work to synthesize a series of MnO_2 materials for application as cathode materials. In a typical experiment, the as-prepared precursor solution was transferred into a 25 ml Teflon-lined stainless steel autoclave, filling it up to 80% of the whole volume. The sealed solution was kept at 150 °C for 8 hours. During this time, different intensities of pulsed magnetic fields (0 T, 2 T, and 4 T) were applied respectively. After the autoclave was cooled down to room temperature naturally, the obtained products were then filtered and washed with distilled water to remove the remaining ions. Finally, the as-prepared materials were dried in a vacuum oven at 80 °C overnight.

3. 3 Electrode Preparation and Cell Fabrication

To fabricate the electrodes, 70 wt.% active material was mixed with 20 wt.% carbon black and 10 wt.% binder. N-methyl-2-pyrrolidinone (NMP) was used as a dispersant to form the slurries. The electrochemical characterizations were carried out using coin cells. CR 2032 coin-type cells (Figure 3.4) were assembled in an Ar-filled glove box (Mbraun, Unilab, Germany) by stacking a porous polypropylene separator and a lithium foil counter electrode. The electrolyte used was 1 M $LiPF_6$ in a 50:50 (v/v) mixture of ethylene carbonate (EC) and dimethyl carbonate (DMC).

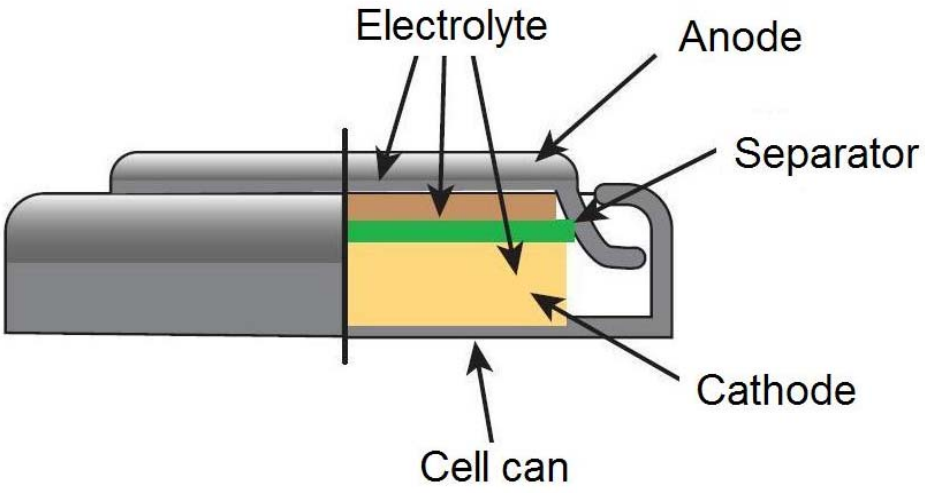

Figure 3.4 Cross-sectional schematic diagram of the coin-type cell.

3. 4 Physical and Structural Characterization

3.4.1 X-ray Diffraction (XRD)

Powder X-ray diffraction (XRD) is a technique used to characterise the crystallographic structure, crystallite size (grain size), and preferred orientation in polycrystalline or powdered solid samples.

XRD was performed using a GBC MMA X-ray generator and diffractometer with Cu Kα radiation. The instrument operates at room temperature, with θ–2θ optics, and is equipped with a 3 kW generator and Cu Kα X-ray tubes. The instrument is fully automated and operates in conjunction with a comprehensive database. The system is interfaced with Visual XRD and Traces version 6.6.10 software designed for graphical processing and manipulation. The tube voltage and current were set at 40 kV and 25 mA, respectively.

3.4.2 Scanning Electron Microscopy (SEM)

Scanning Electron Microscopy (SEM) is used primarily to observe electrode surface topography or the morphology of powder samples.

Sample morphologies were investigated using a JEOL JEM-3000 (30 kV) SEM. Some of the higher resolution SEM images in this research work were obtained by using a field emission scanning electron microscope (FE-SEM), a JEOL JSM-7500FA.

3.4.3 Transmission Electron Microscopy (TEM)

Transmission Electron Microscopy (TEM) is a microscopy technique whereby a beam of electrons is transmitted through an ultra-thin specimen, interacting with the specimen as it passes through. An image is formed from the interaction of the electrons transmitted through the specimen; the image is magnified and focused onto an imaging device, such as a fluorescent screen, or on a layer of photographic film, or is detected by a sensor such as a CCD camera. TEM is capable of imaging at a significantly higher resolution than light microscopes.

TEM investigations were performed using a JEOL 2011 (200 kV) analytical electron microscope and also a Zeiss microscope, a 912 Omega with ProScan, and a slow scan charge-coupled device camera at 100 kV (ETH Zurich). TEM samples were prepared by deposition of ground particles onto lacy carbon support films.

3.4.4 Raman Spectroscopy

Raman spectroscopy is a spectroscopic technique used to study vibrational, rotational, and other low-frequency modes in a system and can be used as a complementary tool to XRD.

The Raman spectrometer used in this study was a JOBIN YVON HR800 Confocal Raman system with 632.8 nm diode laser excitation on a 300 lines/mm grating at room temperature.

3.4.5 Thermogravimetric Analysis (TGA)

Thermogravimetric Analysis (TGA) is a characterization method that is performed on samples to determine changes in weight in relation to change in temperature. The precise weight of the disordered carbon contents in materials was determined by this method. In the experiments, TGA was performed using METTLER TOLEDO TGA/DSC 1 equipment with microsized aluminium oxide crucibles (70 μl).

3.4.6 Brunauer-Emmett-Teller (BET) Method

Specific surface areas of the nanostructured materials were measured with a Quantachrome Nova 1000 nitrogen gas analyzer using the Brunauer-Emmett-Teller (BET) method. The BET specific surface area was determined through a 15-points nitrogen adsorption isotherm at 77 K after degassing the powder samples with nitrogen at 150 ^{o}C.

3. 5 Electrochemical Characterization

3.5.1 Cyclic Voltammetry (CV)

Cyclic voltammetry (CV) is a type of potentiodynamic electrochemical measurement. In a CV experiment, the cell is cycled in a potential window, where the working electrode potential is ramped linearly versus time, as with linear sweep voltammetry. Cyclic voltammetry takes the experiment a step farther than linear sweep voltammetry, which ends when it reaches a set potential. When the set potential is reached in cyclic voltammetry, the working electrode's potential ramp is inverted.

CV is a widely used method for studying electrode processes, especially for providing insights into the nature of processes beyond the electron-transfer reaction. It was used in this research work to study the electrochemical properties of electrodes made from different as-prepared materials. In a typical experiment, the CV testing was conducted by measuring the I-V response at a scan rate of 0.1 mV s^{-1} within the set electrochemical window using a CH Instruments model 660C electrochemical workstation. Parameters were optimized within these ranges depending upon the materials under investigation.

3.5.2 Galvanostatic Charge and Discharge Testing

Charge and discharge cycles of the coin cells were measured using various voltage cut-offs on a Land battery test system at different constant current densities. The rate of the charge and discharge was selected depending upon the theoretical capacity of the material under investigation.

3.5.3 Electrochemical Impedance Spectroscopy (EIS)

In this study, electrochemical impedance spectroscopy was applied to investigate the electrochemical behaviour of the as-obtained materials. In a typical experiment, ac impedance spectroscopy measurements were carried out using a Princeton Applied Research PARSTAT 2273 instrument with Power Suite software package by applying a sine wave of 5 mV amplitude over a frequency range of 100.00 kHz to 0.01 Hz. All impedance measurements were carried out in the discharged state of the cells.

CHAPTER 4 NANOCRYSTALLINE NICKEL OXIDE HOLLOW SPHERES IN CONJUNCTION WITH CMC BINDER AS ANODE MATERIALS FOR LITHIUM-ION BATTERIES

4. 1 Introduction

Although carbon-based materials are the accepted anode used in the majority of commercial lithium-ion batteries, various new higher capacity anode materials are still being studied to meet the increasing energy demands of modern devices, especially electric and hybrid electric vehicles. Among the most attractive candidates, transition-metal oxides could be a new class of promising anode materials for lithium-ion batteries. The transition metal oxides react reversibly with lithium in lithium cells below 1.5 V and demonstrate large capacity (about 700 mAh g^{-1}) and long cycle life [29]. Nickel oxide, NiO, has recently been intensively studied as an anode material.

NiO can be prepared through various methods, such as microwave-assisted and liquid oxidation combination techniques [63], the plasma assisted oxidation method [64], and the molten-salt assisted oxidation route [65]. These preparation methods are, however, very complicated and difficult to control. The spray pyrolysis technique, by comparison, has several advantages. It represents a simple and low-cost alternative for producing large-scale submicron-/nano-particles with controlled

composition and morphology, good crystallinity, and uniform size distribution, all of which can be readily obtained in only one step.

In order to enhance the performance of lithium-ion batteries, researchers and battery manufacturers are not only trying to create new electrode materials, but also searching for new binders, since battery efficiency is strongly dependent on the electrode engineering [57, 59]. Recent studies have shown that some binders used for electrode preparation influence the electrochemical performance of the batteries [66, 67]. The most common binder used in Li-ion batteries is poly(vinylidene) fluoride, PVDF. The mechanical and electrochemical properties of PVDF are a good compromise between the multiple criteria described above. However, using PVDF has the following drawbacks:

(a) PVDF is only soluble in organic solvents, and it is expensive and dangerous to humans and the environment;
(b) Control of the humidity (less than 2%) is needed during the electrode preparation.

Recently, aqueous binders have gradually replaced PVDF binder for the anode material [68, 69, 70, 71] . The advantages of aqueous binders are [72]: (1) low cost, (2) no pollution problems, and (3) no requirement for strict control of the processing humidity. Among the various water soluble binders, carboxymethyl cellulose (CMC) is the most attractive binder for improving battery performance. CMC is soluble in environmentally friendly solvents such as water [73], which is of importance for future electrode production.

In this chapter, a simple spray pyrolysis method to prepare hollow spherical NiO is described. NiO electrode using CMC binder is being studied for the first time. The capacity and cycling stability of the NiO electrode using the CMC binder are improved significantly compared with the results published previously, in which the NiO electrodes contained PVDF as the binder [74].

4. 2 Experimental

4.2.1 Synthesis of Hollow Spherical NiO

Nanocrystalline NiO powders were synthesized by a spray pyrolysis method [75]. Nickel oxide powder was prepared using 0.1, 0.3, and 0.5 mol L^{-1} aqueous solutions of nickel nitrate hexahydrate, $Ni(NO_3)_2 \cdot 6H_2O$ (Aldrich Chemicals). The solution was peristaltically pumped into a three-zone spray pyrolysis furnace with the operating temperature at 700 °C, using compressed air as the carrier gas. The resultant powder was separated from the hot gas stream via a collecting jar and collected into airtight sample bottles.

4.2.2 Structural and Electrochemical Characterization

Phase analysis was performed by powder X-ray diffraction (XRD) using a Phillips 1730 X-ray generator and diffractometer with Cu Kα radiation. The morphologies of the NiO powders were investigated by scanning electron microscopy (SEM; JEOL JEM-3000, 30 kV), field emission SEM (FE-SEM; JEOL JSM-7500F), and transmission electron microscopy (TEM; JEOL 2011, 200 kV). The electrodes with different binders were studied by SEM before and after cycling.

To fabricate the NiO electrodes, 70 wt% NiO powder was mixed with 20 wt% carbon black and 10 wt% binder, which was either CMC or PVDF, using de-ionized water or N-methyl-2-pyrrolidinone (NMP) as the respective solvents. The electrochemical characterizations were carried out using CR 2032 coin-type cells, which were assembled in an Ar-filled glove box (Mbraun, Unilab, Germany) by stacking the NiO anodes with a porous polypropylene separator and a lithium foil counter and reference electrode. The electrolyte used was 1 M $LiPF_6$ in a 50:50 (v/v) mixture of ethylene carbonate (EC) and dimethyl carbonate (DMC). The cells were galvanostatically discharged and charged at a current density of 100 mA g^{-1}. The discharge capacities are based on the amount of active material in the electrodes.

4. 3 Results and Discussion

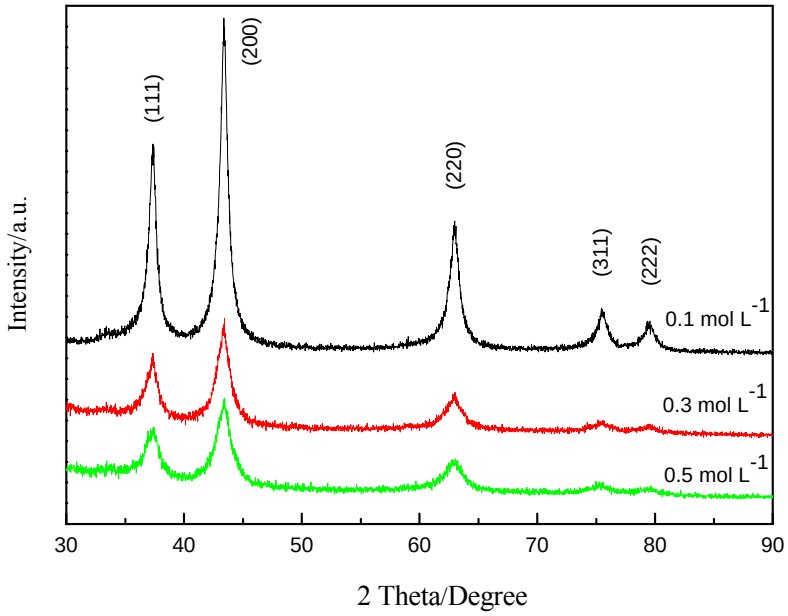

Figure 4.1 X-ray diffraction patterns for NiO powders from spray pyrolysis solutions at different concentrations.

Figure 4.1 shows the XRD patterns of the NiO powders prepared by the spray pyrolysis method at 700 °C using the solutions of $Ni(NO_3)_2 \cdot 6H_2O$ with concentrations of 0.1, 0.3, and 0.5 mol L^{-1}, respectively. All the diffraction peaks correspond well with standard crystallographic data (Joint Committee on Powder Diffraction Standards (JCPDS) File No. 04-0835). The structure is that of a cubic unit cell with diffraction peaks at 37.38°, 43.38°, 62.92°, 75.28°, and 79.48°. The X-ray diffraction peaks for the NiO powders are very broad, indicating their nanocrystalline nature. The average crystal sizes of the NiO powders were determined by using the Traces software package and the Scherrer formula. The crystal sizes are 10.52, 3.99, and 3.27 nm for the NiO samples sprayed from solutions of 0.1, 0.3, and 0.5 mol L^{-1}, respectively. The crystal size of the NiO powders was reduced when the concentration was increased. The results indicate that pure nanocrystalline NiO powders with very small crystal sizes can be prepared by the simple spray pyrolysis method.

An SEM image of the NiO powders prepared from the 0.3 M solution is shown in Figure 4.2(a). The particles are mainly spherical agglomerates, which is a typical structure for this spray process, with sizes in the range of 2-4 microns. From the broken spherical particles, it can be seen that the particles are spherical hollow balls. It also can be seen from FE-SEM (Figure 4.2(b)) that the wall thickness ranges from 300-500 nm. The spherical hollow balls are composed of small spheroidal particles with sizes of 20-50 nm. The hollow spherical structure is further confirmed by TEM (Figure 4.2(c)). In the selected-area electron diffraction (SAED) pattern presented in Figure 4.2(d), all of the electron diffraction rings can be indexed to cubic phase NiO,

which also agrees very well with the XRD analysis. The Brunauer-Emmett-Teller (BET) results made it clear that an increase in the concentration of the precursor solution caused a pronounced decrease in the BET specific surface area, S_{BET}. The powder obtained from the 0.1 mol L^{-1} solution exhibits a remarkably high S_{BET} value of 42.4 m^2 g^{-1}. The powders prepared using 0.3 and 0.5 mol L^{-1} solutions have values of only 10.5 and 9.7 m^2 g^{-1}, respectively.

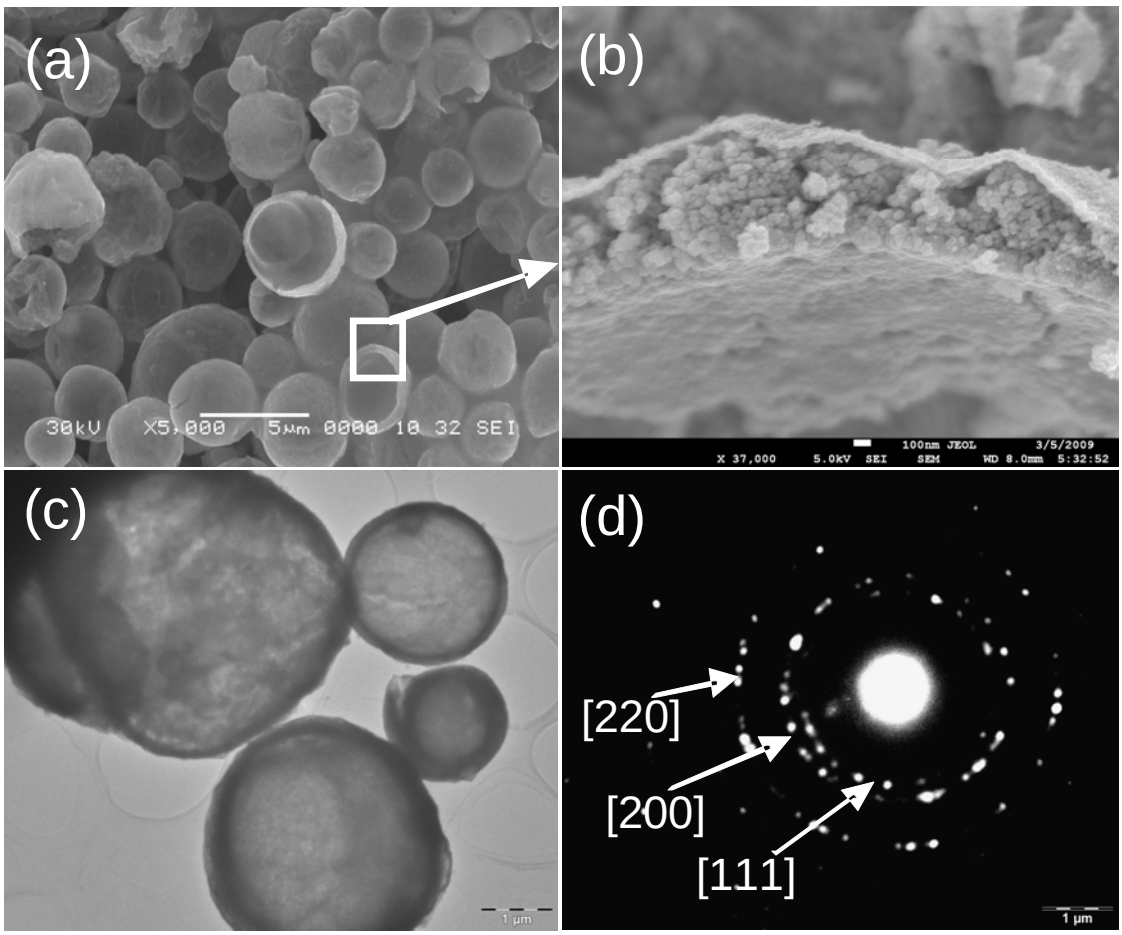

Figure 4.2 Images of NiO powder made from 0.3 M precursor: (a) SEM, (b) FE-SEM, (c) TEM, and (d) corresponding SAED pattern to (c).

Figure 4.3 shows discharge capacities versus cycle number for cells made using NiO electrodes, where the NiO was sprayed from different concentrations of the precursor

solution, and the two different binders. When using PVDF as a binder, it was found that the capacities for all the samples were high for the first few cycles; however, the discharge capacities decreased dramatically over 10 cycles and only showed 250, 157, and 102 mAh g^{-1} (for the 0.1, 0.3 and 0.5 mol L^{-1} precursor concentrations, respectively) after 40 cycles. This phenomenon has been reported in previous publications [74].

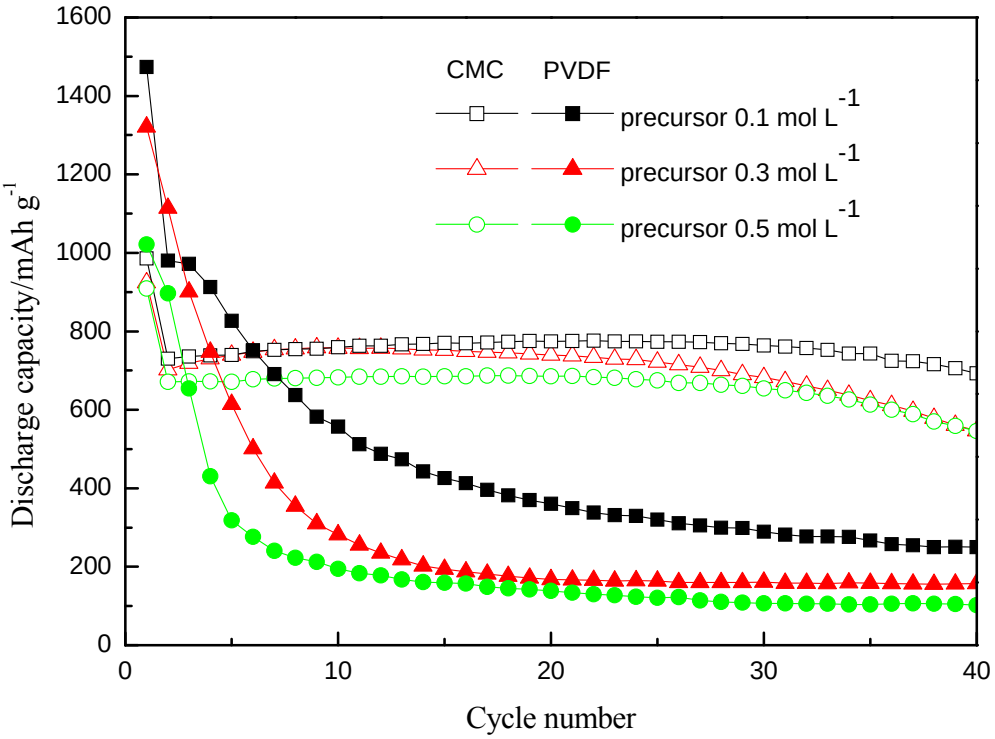

Figure 4.3 Discharge capacities vs. cycle number for NiO electrodes made from spray solutions at different concentrations with PVDF and CMC binders.

In order to improve the cycling stability of the NiO samples prepared by the spray pyrolysis method, CMC binder was tested using the as-prepared NiO powders. The cycling stabilities of the cells with CMC are obviously improved. The NiO electrodes made from 0.1, 0.3 and 0.5 mol L^{-1} precursor concentrations using CMC as the

binder demonstrate capacities as high as 693, 547 and 545 mAh g^{-1}, respectively, after 40 cycles, which is an obvious improvement compared to the electrodes using PVDF binder. Typical charge-discharge curves of the cells made from the 0.3 mol L^{-1} precursor concentration with the two different binders are presented in Figure 4.4. The first discharge capacities of the NiO electrodes with PVDF and CMC binders are 1320 and 924 mAh g^{-1}, and the first charge capacities of these NiO electrodes are 747 and 698 mAh g^{-1}, respectively. The irreversible capacity loss between the first discharge and the first charge is about 43% and 24% for the electrodes with PVDF and CMC binders, respectively. These results confirm that the binder is an important issue affecting the cycling stability [67, 71].

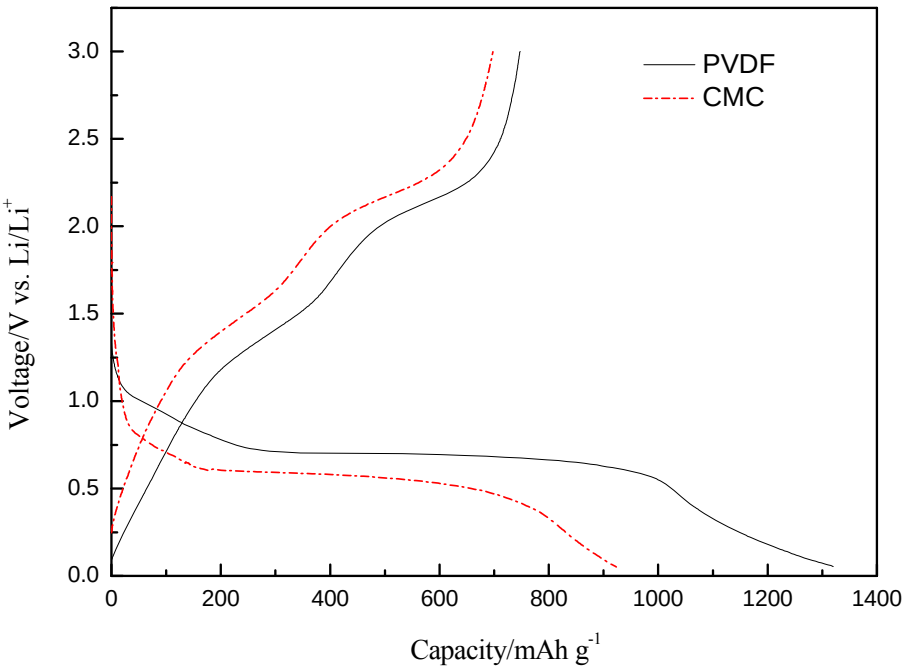

Figure 4.4 Typical charge-discharge curves for NiO electrodes (0.3 mol L-1) with CMC and PVDF binders.

To investigate the relationship between the ac impedance spectra and the cycling behaviors of electrodes with different binders, we carried out electrochemical impedance spectroscopy (EIS) tests on the NiO electrodes made from the 0.3 mol L^{-1} precursor solution before cycling, after 5 charge-discharge cycles, and after 40 cycles. The Nyquist impedance plots of the NiO electrodes with different binders before and after cycling are presented in Figure 4.5. Generally, the high frequency semicircle and the semicircle in the medium-frequency region are attributed to the solid electrolyte interphase (SEI) film and/or contact resistance, and the Li^+ charge-transfer impedance on the electrode/electrolyte interface, respectively. The inclined line at an approximate 45° angle to the real axis corresponds to the lithium-diffusion processes within the electrode [76]. From Figure 4.5(a), it can be clearly seen that the diameters of the semicircles in the medium-frequency region are similar before cycling for the two electrodes, regardless of the binder. However, the diameters of the semicircles for electrodes with CMC binder are smaller than for the electrodes with PVDF binder after 5 and 40 cycles (Figure 4.5(b)). The results indicate that the charge-transfer resistance of the cell with NiO/CMC electrode is much lower than that of the cell made from NiO/PVDF. This phenomenon may be the reason why the capacity and cycling stability of the cell with CMC are much better compared to the cell with PVDF binder (see Figure 4.3).

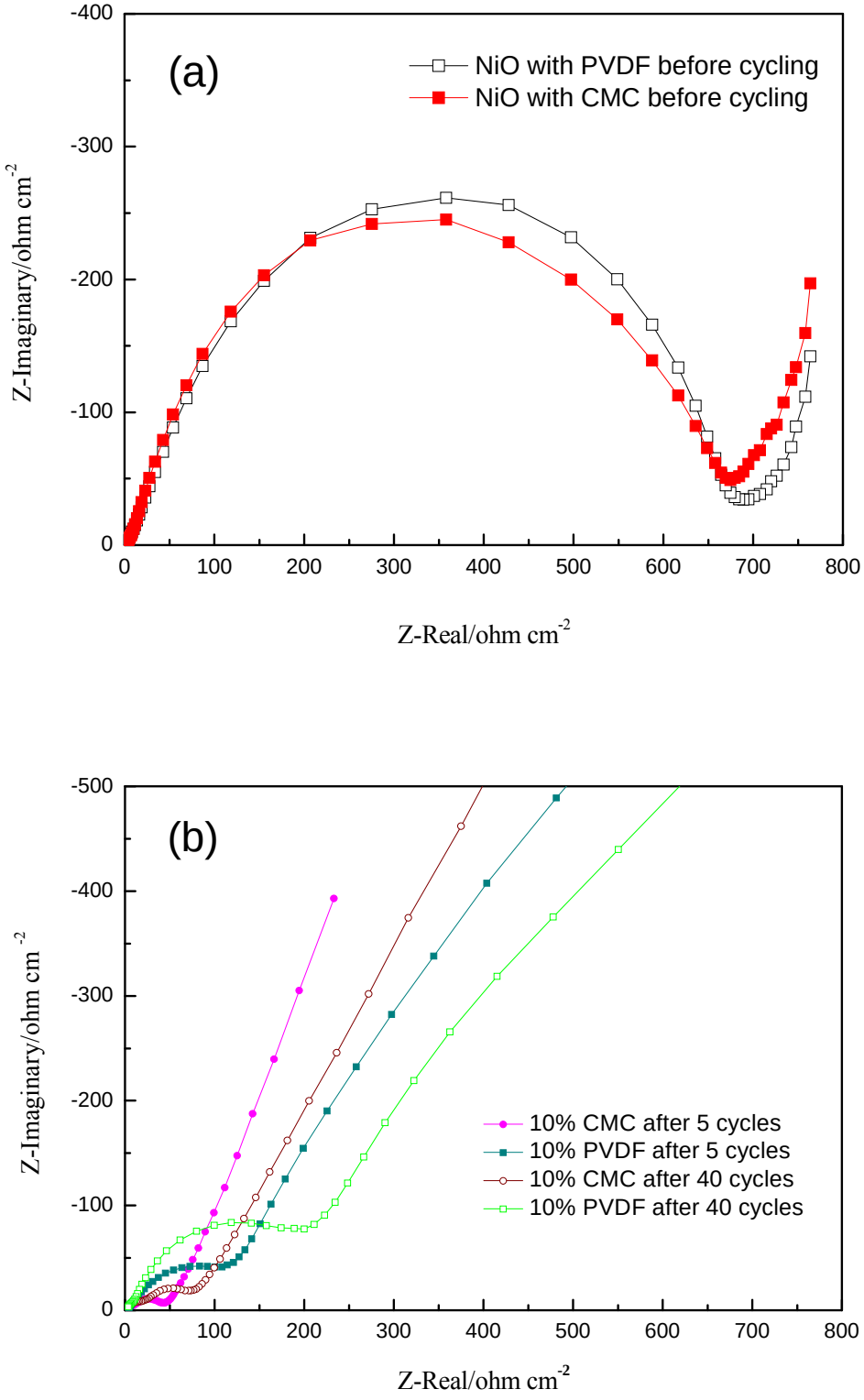

Figure 4.5 Nyquist impedance plots of NiO electrodes (0.3 mol L^{-1}) with different binders (a) before and (b) after cycling.

In order to explore the reasons why the charge-transfer resistance is higher in the cell with PVDF binder after cycling, a morphological study of the electrodes before cycling and after 40 cycles was conducted (Figure 4.6). As can be seen, the

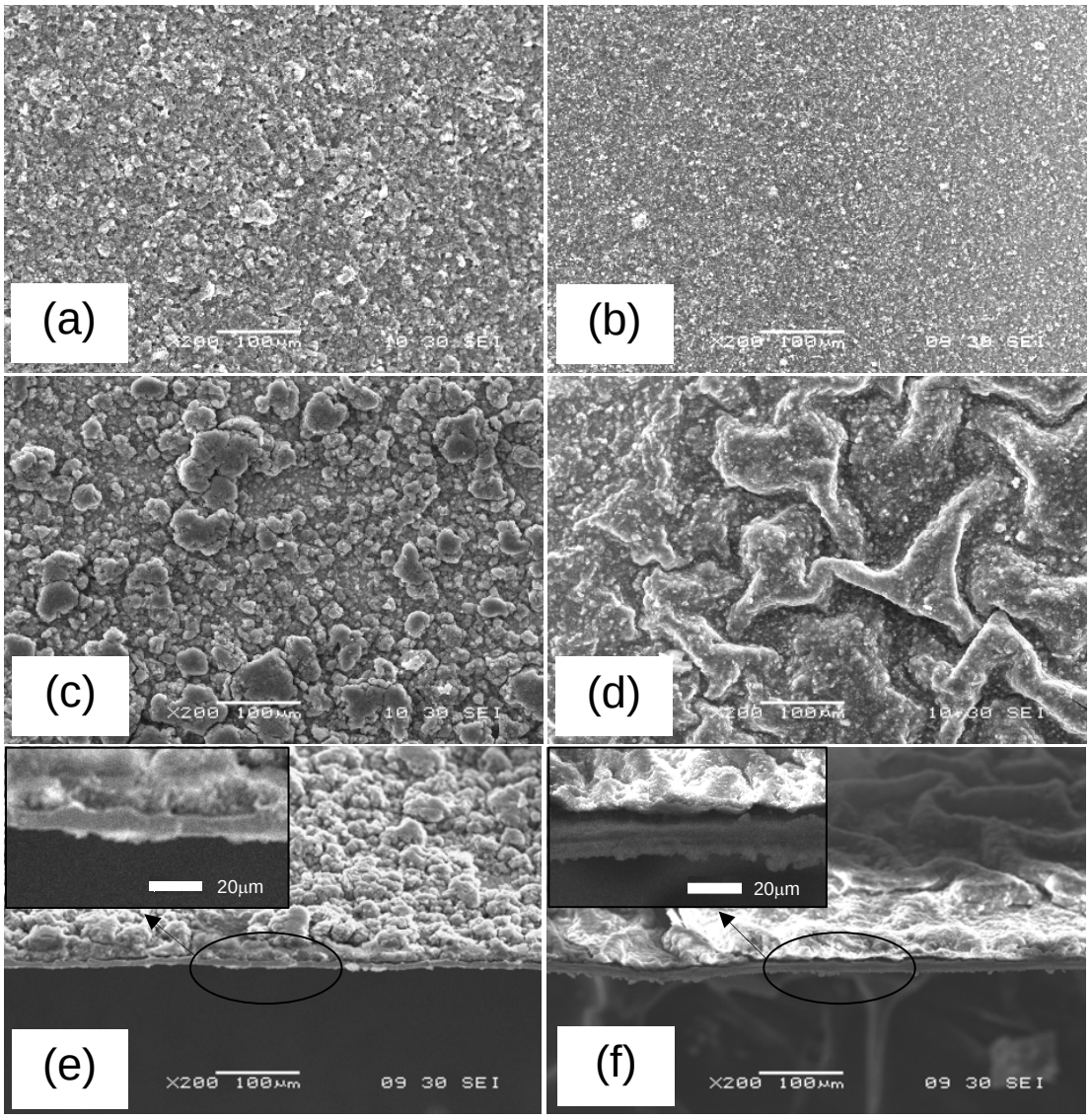

Figure 4.6 SEM images of NiO electrodes (0.3 mol L^{-1}) with CMC binder (left) and PVDF binder (right): (a-b) before cycling, (c-d) after cycling, (e-f) cross-sections of electrodes after cycling. Insets in (e) and (f) show enlargements of the indicated areas.

electrode material is expanded and creased after cycling for the cell with PVDF binder, while the electrode particles of the cell with CMC are just slightly

agglomerated compared to the electrode before cycling (Figure 4.6(a)-(d)). The images of the electrode cross-sections show that the electrode material with CMC has remained adhered to the copper foil, while a big gap is found between the active material and the substrate for the electrode with PVDF after 40 cycles (Figure 4.6(e) and (f)).

4. 4 Chapter Summary

Nanocrystalline NiO hollow spheres were synthesized by the spray pyrolysis method using different concentrations of precursor solution and tested as anode materials with CMC and PVDF binders. The as-prepared material obtained from a lower concentration of precursor has a larger BET specific surface area and therefore gives better electrochemical performance. It was also found that the capacity and cycling stability of the electrode using CMC binder are significantly improved compared to the electrode with PVDF binder. The preliminary results studied here provide useful information for further research on exploring new environmentally friendly water soluble binders to replace the conventional organic solvent based binders for battery applications.

CHAPTER 5 SPRAY PYROLYSIS SYNTHESIZED COPPER OXIDE-CARBON COMPOSITE COMBINED WITH CMC BINDER AS ANODE FOR LITHIUM-ION BATTERIES

5. 1 Introduction

The demand for a more powerful lithium-ion battery system has become much stronger in the last few decades because of the rapid development of modern portable electronic devices [1, 3, 7, 77]. Recently, materials based on transition-metal oxides (MO, M = Co, Ni, Cu, Fe…) have attracted researchers' intensive interest as alternatives to anode materials, mainly due to their high theoretical capacities compared to the commercial graphite anode [29, 30]. Among them, copper oxide (CuO) is a very promising candidate (with a capacity of 675 mAh g^{-1}, theoretically), which has the advantages of high safety, low cost, and environment-friendliness [78, 79]. Nevertheless, as has been reported previously, anodes based on pure transition-metal oxide materials suffer from poor cycling performance due to various factors, such as low conductivity, large volume change, and the serious agglomeration of the materials during the charge and discharge cycles [80, 81]. To overcome these drawbacks, carbon coated composites of the materials can be very effective. This is because carbon is a very good conductive additive and hence can improve the conductivity of the materials. Hydrothermal, calcination, and other methods have been used for the carbon coating of transition-metal oxide composites such as NiO-C and Fe_2O_3-C for lithium-ion batteries [76, 82, 83, 84]. However, no exploratory work has been done on carbon coating modification of CuO for use in lithium-ion

batteries, and the above-mentioned methods have obvious disadvantages besides, such as low productivity, as well as being time-consuming and difficult to control, making them unsuitable for industry-scale use. The spray pyrolysis method is a very fast and easy-to-control technique, especially for large-scale fabrication of materials for industry [85]. Particle size can be easily controlled by changing the spray parameters and the concentration of the precursor solution. Therefore, it could be considered as a new prospect for the carbon-coating work.

Choosing proper binders for electrode materials is another very important issue for researchers and battery manufacturers, attracting considerable research interest, since battery performance strongly depends on the electrode engineering [86]. Li et al. reported that Fe_2O_3 electrodes using carboxymethyl cellulose (CMC) binder showed better cycling performance (about 800 mAh g^{-1} for 100 cycles) compared to electrodes made from conventional poly(vinylidene) fluoride (PVDF) binder [60]. Chou et al. also reported that SnO_2 electrode with CMC binder gave better performance than with PVDF [61]. CMC has other obvious advantages [87]: (i) the cost is low; (ii) it is an aqueous binder, which makes the electrode fabrication process more environmentally friendly; (iii) there is no requirement for strict control of the processing humidity, which is of great importance for battery production.

Herein, nanostructured hollow spherical CuO-carbon composite was prepared by a simple one-step spray pyrolysis method and tested as anode material compared with the bare CuO material which was obtained under the same conditions. Aqueous CMC binder was also examined during the electrode fabrication process in comparison with the traditional binder, PVDF.

5. 2 Experimental

5.2.1 Synthesis of the Materials

CuO-carbon composites were synthesized using a spray pyrolysis method. In a typical experiment, the precursor solution contains 0.25 M $Cu(NO_3)_2$ ($Cu(NO_3)_2 \cdot 3H_2O$, 99.5 %, BDH) with 0.06 or 0.14 M sucrose ($C_{12}H_{22}O_{11}$, 98%, Aldrich) as carbon source. The solution was pumped into a three-zone spray pyrolysis furnace with an operating temperature of 700 °C, using compressed air as the carrier gas. $Cu(NO_3)_2$ was decomposed to form CuO, and the sucrose was transformed into amorphous carbon. The resultant powders, designated CuO:C=70:30 and CuO:C=50:50, respectively, were separated from the hot gas stream via a cyclone/collecting jar, and collected into airtight sample bottles. The pure CuO was also prepared for comparison under the same condition with no sucrose in the precursor solution.

5.2.2 Structural and Electrochemical Characterization

Phase analysis was performed by powder X-ray diffraction (XRD) using a GBC MMA X-ray generator and diffractometer with Cu Kα radiation. The morphologies of the as-obtained powders were investigated by scanning electron microscopy (SEM; JEOL JEM-3000, 30 kV) and field emission SEM (FE-SEM; JEOL JSM-7500FA). Thermogravimetric analysis (TGA) was performed using a Mettler Toledo TGA/DSC 1 STAR System to examine the carbon content. Brunauer-Emmett-Teller

(BET) specific surface areas of the samples were measured using a Quantachrome Nova 1000 system.

To fabricate the electrodes, 70 wt% active materials was mixed with 20 wt% carbon black and 10 wt% binder, which was either CMC or PVDF, using de-ionized water or N-methyl-2-pyrrolidinone (NMP) as the respective solvents. The electrochemical characterizations were carried out using CR 2032 coin-type cells, which were assembled in an Ar-filled glove box (Mbraun, Unilab, Germany) by stacking the anodes with a porous polypropylene separator and a lithium foil counter and reference electrode. The electrolyte used was 1 M $LiPF_6$ in a 50:50 (v/v) mixture of ethylene carbonate (EC) and dimethyl carbonate (DMC). The cells were galvanostatically discharged and charged within a voltage window of 0.01-3.0 V (vs. Li/Li^+) at different current densities and a temperature of 20 ^oC. The discharge capacities are based on the amount of active material in the electrodes.

5. 3 Results and Discussion

5.3.1 Physical and Structural Characterization

The X-ray diffraction patterns are shown in Figure 5.1. It can be observed that the diffraction peaks of the pure CuO and CuO:C=70:30 samples can be indexed to CuO (JCPDS 041-0254). For the CuO:C=50:50 sample, it can be observed that there are peaks at 36.5° and 42.4° that belongs to Cu_2O (JCPDS 05-0667), which resulted from the deoxidation reaction of the carbon source during the spray pyrolysis process. These results demonstrated that the CuO-carbon composite can be synthesized via the spray pyrolysis method, but CuO can be partially deoxidized by

the high carbon source content during the carbon coating process via the spray pyrolysis method at the temperature of 700 ºC.

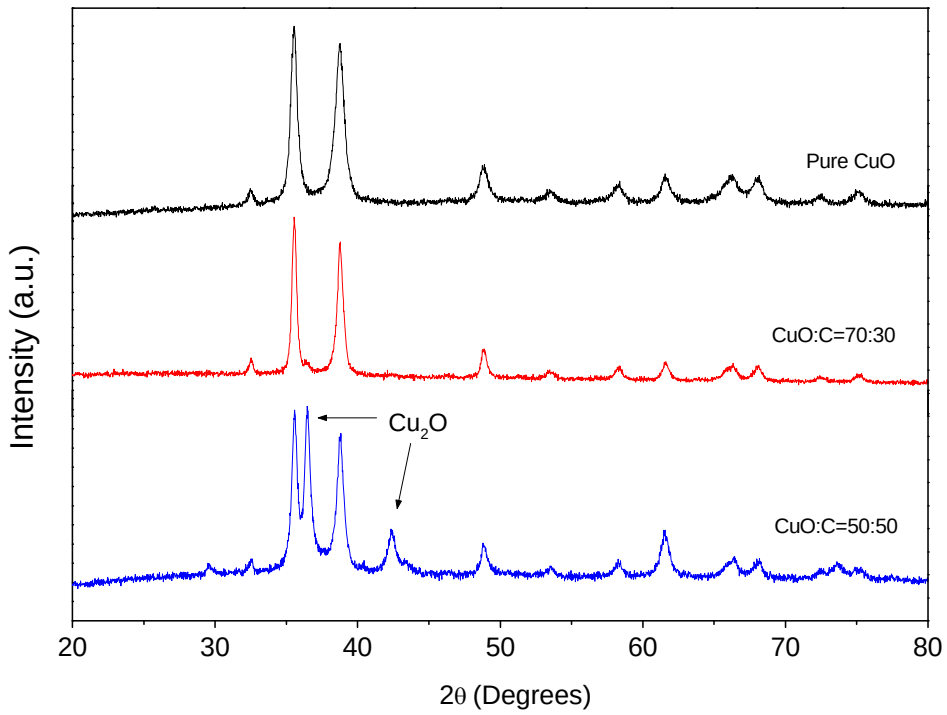

Figure 5.1 XRD patterns for the as-prepared (a) bare CuO and (b) CuO-carbon composite materials.

To investigate the morphology of the products, SEM images were collected for the pure CuO and CuO:C=70:30 composite. From Figure 5.2 (a) and (b), it can be clearly seen that the surface of the spherical structures for the pure CuO sample is very smooth, but the spherical shells are rough and gully-like for the CuO-carbon composite sample. The sizes of the sphere for both of the two samples are mainly the same, between 2-3 μm in diameter. From the FESEM images (Figure 5.2 (c) and (d)) it can be clearly seen that spheres consist of small spheroidal particles. These small

particles in the carbon coated material (diameter: 30 nm) are more uniform than those in the pure CuO material (diameter: 30-50 nm). A difference also appears in the thickness of the shell, which is approximately 93 nm for the pure CuO sample, and only 40 nm, which is less than half of that, for the CuO-carbon composite sample. Some ridge-like structures are also observed from the inside of the sphere for the composite sample, which match the gully-like shapes in the SEM images (Figure 5.2(b)) very well. The Brunauer–Emmett–Teller (BET) measurements demonstrated that the specific surface area value for the composite sample is higher (96 m^2 g^{-1}) than for the pure CuO sample (90 m^2 g^{-1}).

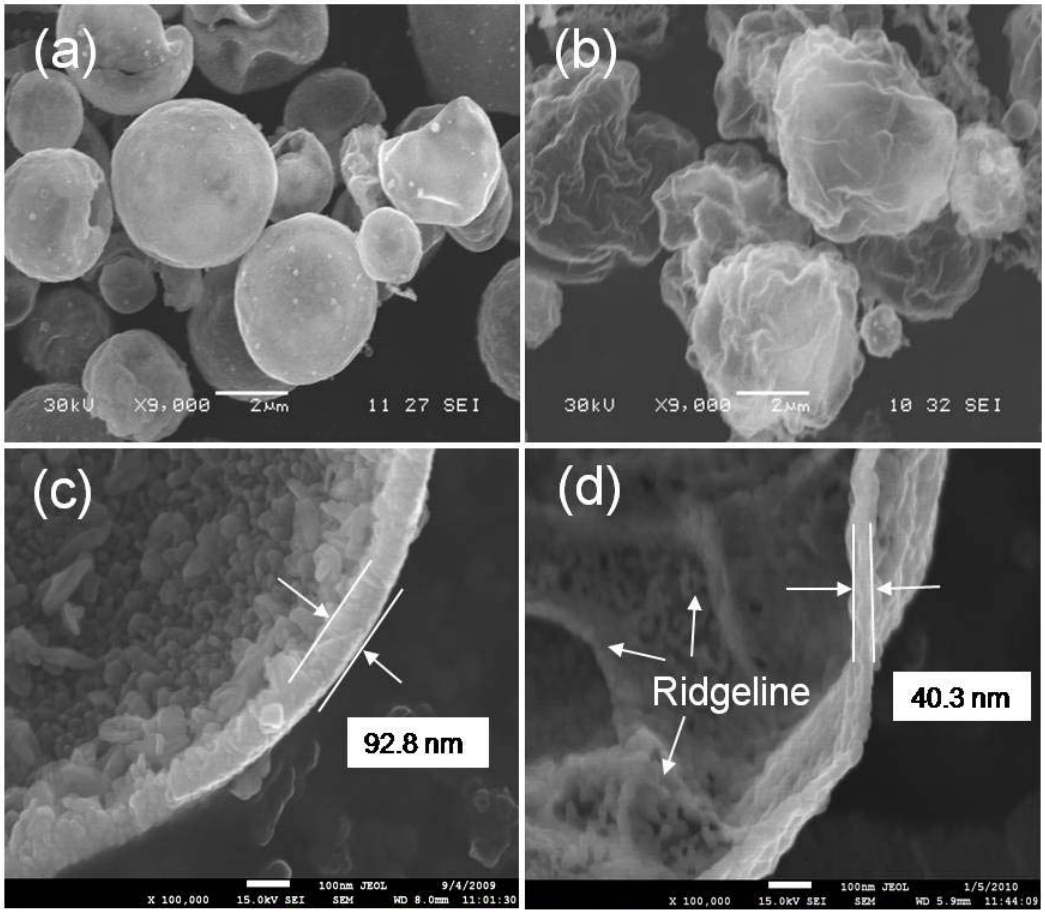

Figure 5.2 SEM images of (a) pure CuO, (b) CuO:C=70:30 composite, and respective FESEM images (c-d)

An SEM image obtained from the CuO:C=70:30 composite sample with corresponding energy dispersive spectroscopy (EDS) maps for CuO, C, and O is shown in Figure 5.3. The bright regions correspond to the presence of the elements Cu, C, and O, respectively, and indicate that C is uniformly distributed on the CuO spheres.

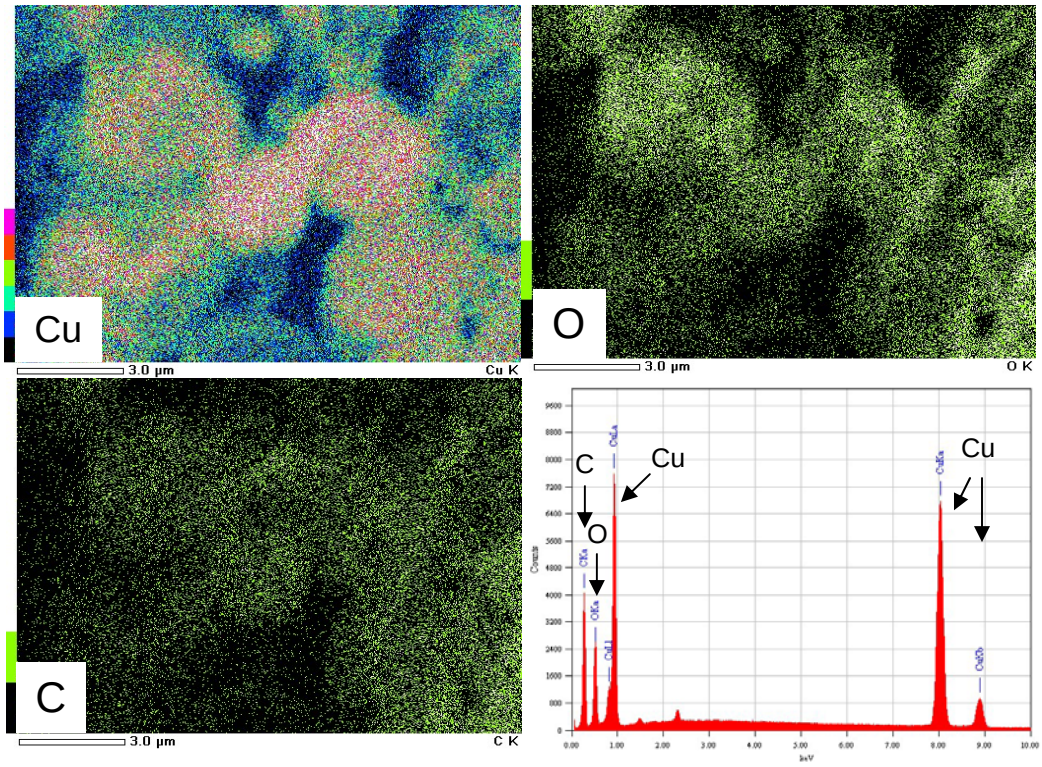

Figure 5.3 EDX mapping for the as-prepared CuO:C=70:30 composite material.

To quantify the weight percentage of carbon in the sample, thermogravimetric analysis (TGA) was also carried out in air (Figure 5.4). The heating temperature was set between 60 and 600 ^{o}C at a rate of 5 ^{o}C min^{-1}. It can be seen from Figure 5.4 that the composite samples show mass loss during heating. As the pure CuO remains stable in the temperature range, any weight change corresponds to the oxidation of

carbon. Therefore, the change in weight before and after the oxidation of carbon directly translates into the amount of carbon in the CuO-carbon composite. With the use of this method, it was estimated that the amount of carbon in the two composites was about 1.3 and 7.9 wt%, respectively. These values of carbon content are much smaller than the theoretical values, which are at 30.3 wt% and 50.4 wt%. These discrepancies are because most of the carbon was burned out into CO or CO_2 during the spray pyrolysis process at 700 ^{o}C. The slightly increase between 300 and 350 ^{o}C for the CuO:C=50:50 curve is because the impurity Cu_2O in the sample oxidized to CuO.

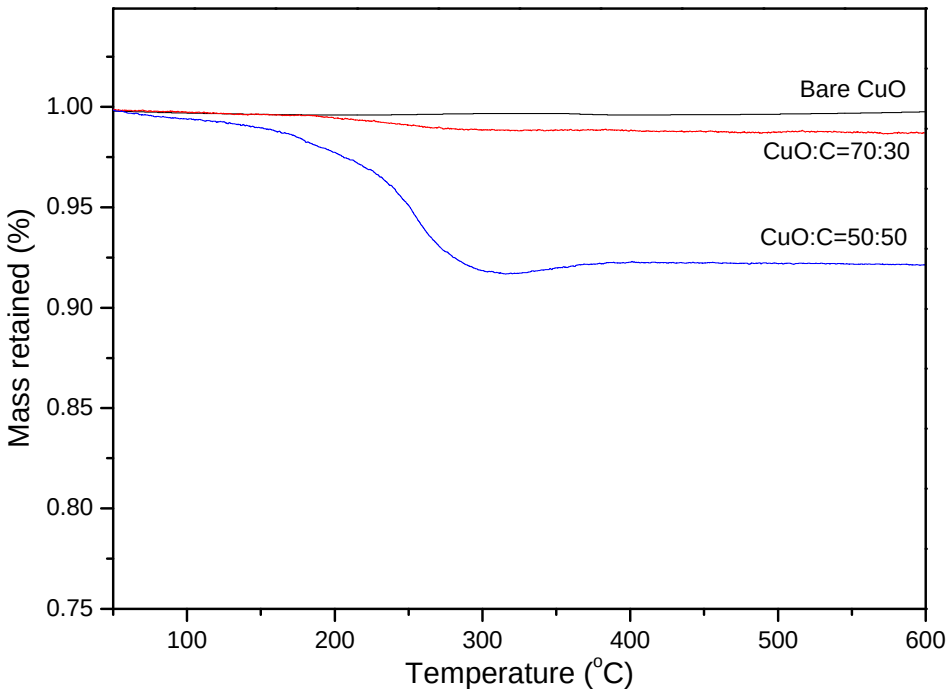

Figure 5.4 TGA curves for the as-prepared materials.

5.3.2 Electrochemical Properties

Cyclic voltammograms, collected at a scan rate of 0.1 mV s^{-1} and at room temperature, of the electrodes made from the as-prepared materials are depicted in Figure 5.5. In the first cycle, there are two cathodic peaks of lithium insertion in both of the electrodes, which are located at around 1.03 and 0.76 V vs. Li/Li^+ in all the voltammograms. At the same time, it is clear that the peak at 1.03 V is much higher for the CuO-carbon sample than for the bare CuO sample, which indicates that the reactivity of the CuO-carbon composite electrode in the lithium cell is higher. In the second cycle, decreases in the peak intensities, indicating irreversible capacity loss, are observed, and a new cathodic peak appears at 2.16 V that is not evident in the first cycle. In the following cycles, there is no further substantial change in the peak potential range and curve shape.

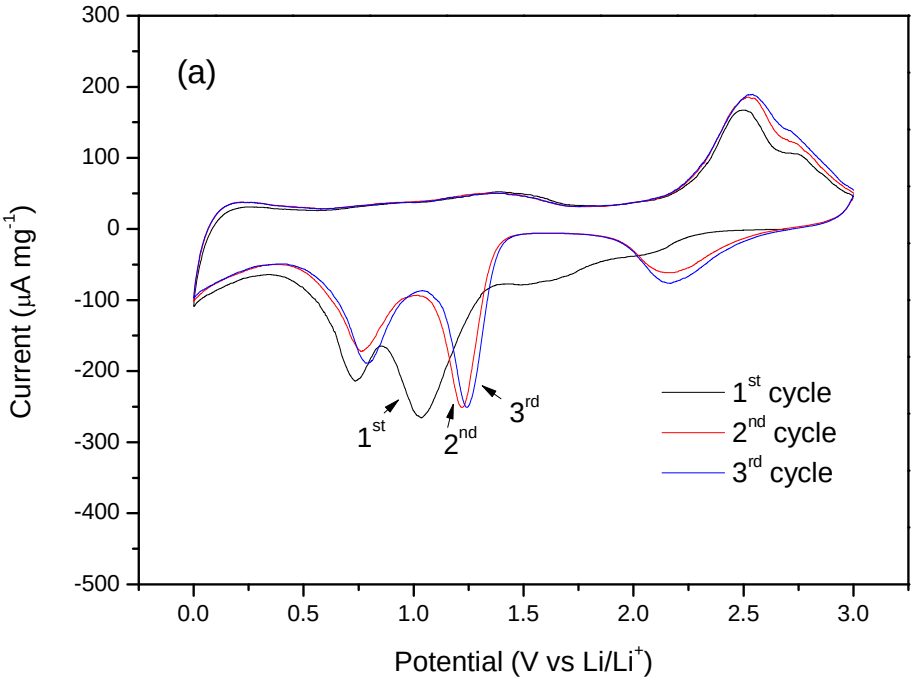

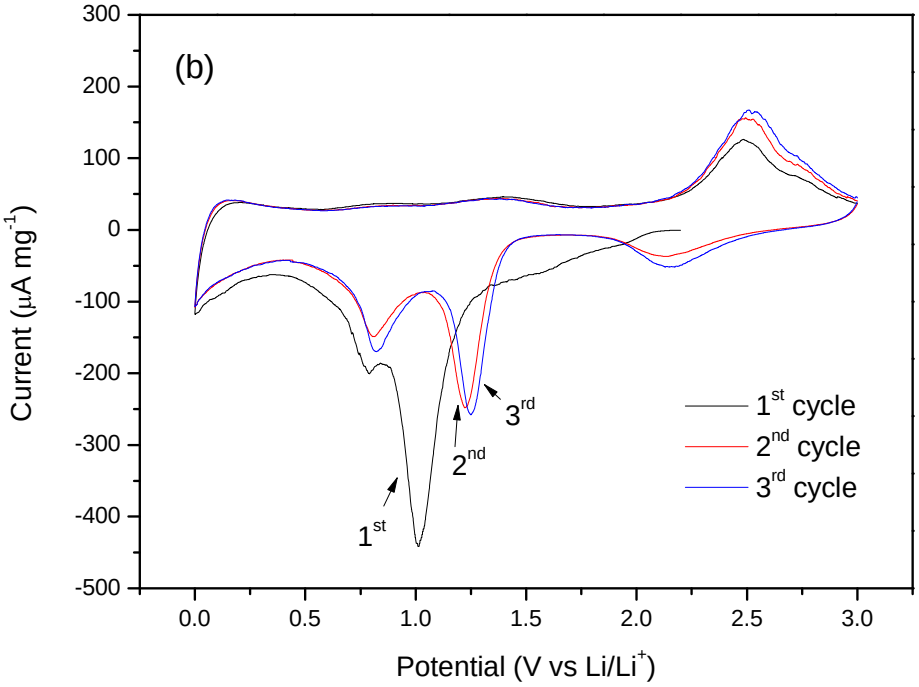

Figure 5.5 Cyclic voltammorgrams of the electrodes made from the as-prepared (a) bare CuO and (b) CuO-carbon materials at a scan rate of 0.1 mV s^{-1}.

Cycling performances for the electrodes made from pure CuO and CuO-carbon composite samples with different binders are shown in Figure 5.6(a). When using PVDF as the binder, it can be clearly seen that the discharge capacity of the cells with CuO:C=70:30 composite electrode is higher than that of the pure sample, but capacity drops very quickly for both samples, with only 283 and 199 mAh g^{-1} retained, respectively, after 100 cycles. When CMC binder was used instead of PVDF, the cycling performances were significantly improved. The CuO:C=70:30 composite electrode maintained a very stable discharge capacity up to 100 cycles (577 mAh g^{-1}), while the performance of the pure sample decreased significantly in the initial 20 cycles, with discharge capacity of 416 mAh g^{-1} after 100 cycles. The CuO:C=50:50 sample has a very stable cycling performance, but the discharge

capacity is lower than for the CuO:C=70:30 sample due to the higher carbon ratio and the Cu_2O impurity. Figure 5.6(b) presents the rate capability of the as-prepared samples in conjunction with CMC binder. The cell was cycled at a rate of 100 mA g^{-1} initially, and then increased to 200, 400, 600, and 800 mA g^{-1}, successively. The results demonstrated that the carbon coated samples have better high rate capabilities than the pure one. The introduction of carbon into CuO spheres can enhance the electronic conductivity within and between the CuO particles.

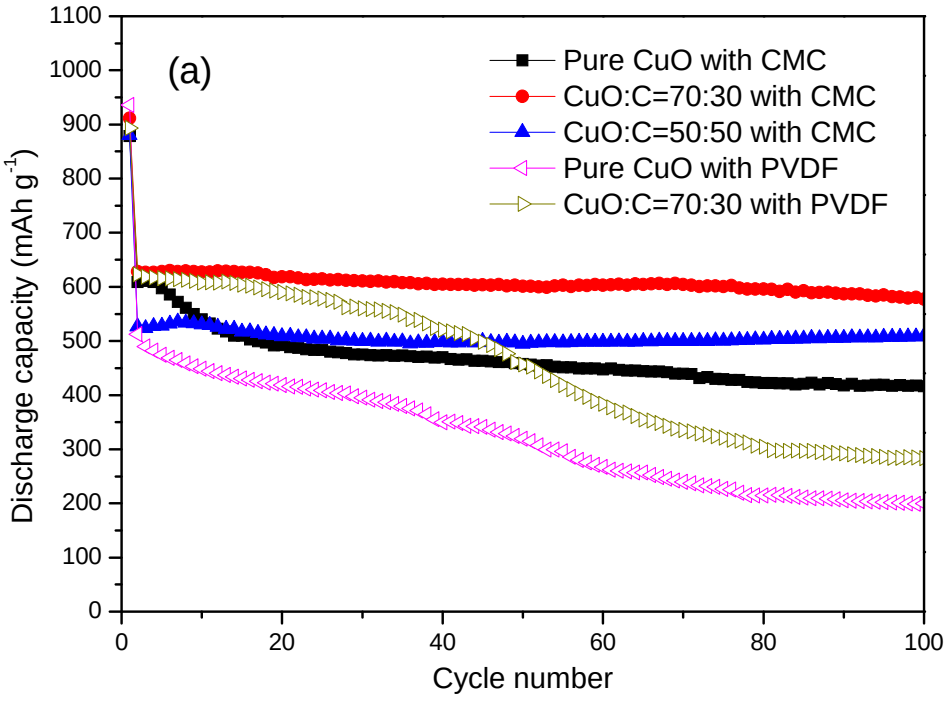

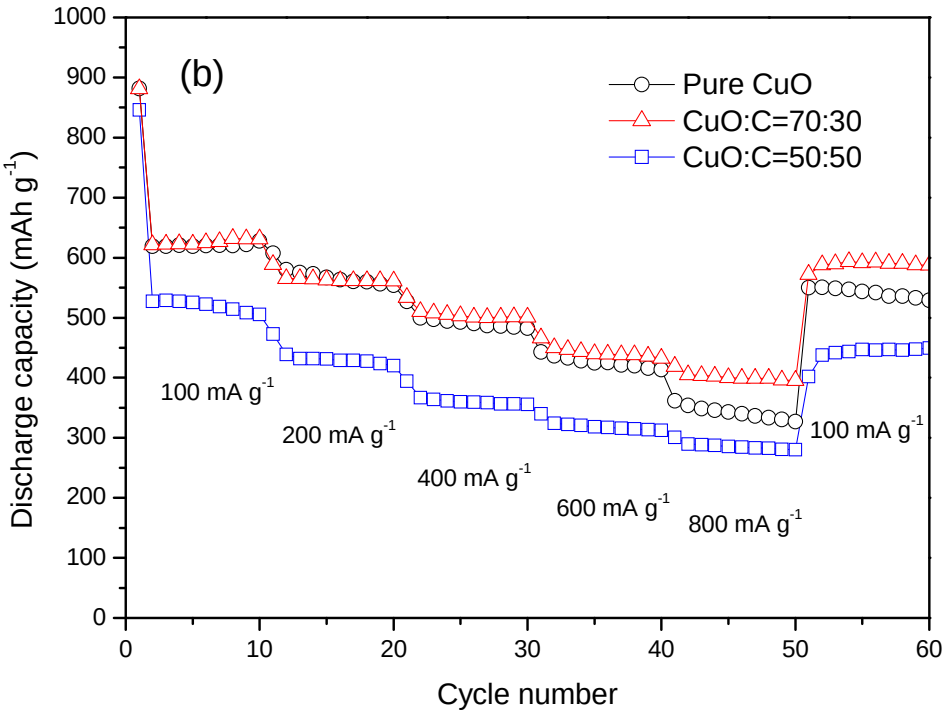

Figure 5.6 (a) Cycling behavior of the samples with CMC or PVDF binders at a scan rate of 100 mA g^{-1}; (b) rate capability of the samples with CMC binder

Electrochemical impedance spectroscopy (EIS) was also performed on the 50th cycle of the electrodes made from pure CuO and CuO:C=70:30 composite combined with CMC and PVDF binders (Figure 5.7). Generally, the high frequency semicircle and the semicircle in the medium-frequency region are attributed to the solid electrolyte interphase (SEI) film and/or contact resistance, and the Li^+ charge-transfer impedance on the electrode/electrolyte interface, respectively. It can be seen that the conductivity of the composite electrode is much lower than that of the pure electrode, from which it can be assumed that the interparticle resistance of the electrode was suppressed by the addition of carbon. In addition, the electrodes with CMC binder show higher conductivities than those with PVDF binder, which is probably due to

the CMC's good internal bonding of the material so that it can survive the large, repeated dimensional changes of the electrode during the charge/discharge process.

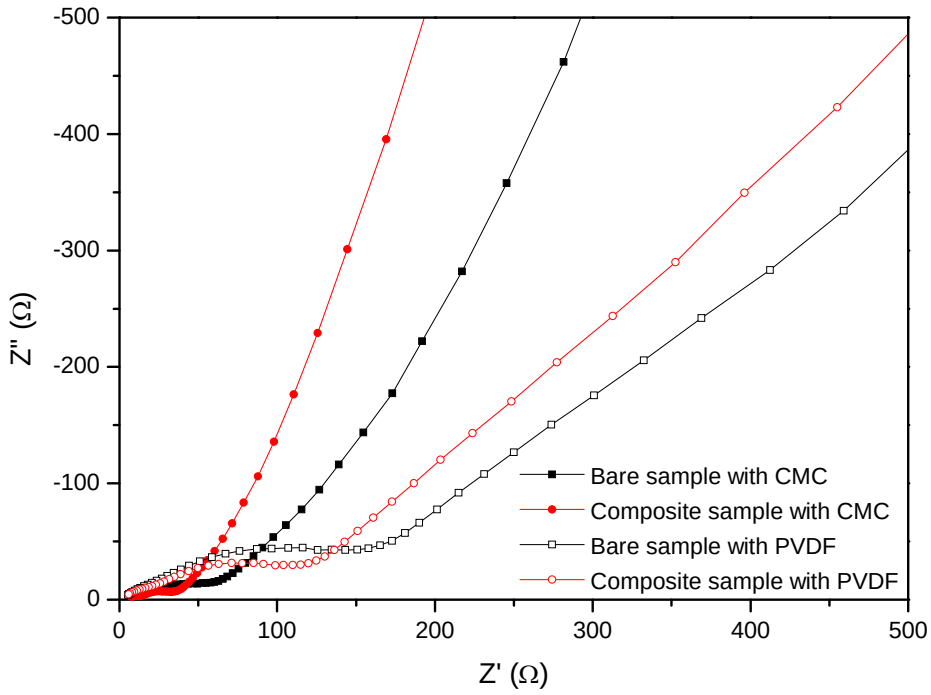

Figure 5.7 Nyquist impedance plots (50th cycle) of the bare CuO and CuO:C=70:30 composite electrodes with different binders.

5. 4 Chapter Summary

In summary, a simple one-step spray pyrolysis method was applied for the synthesis of large-scale production of nanostructured hollow spherical bare CuO and CuO-carbon composite electrode material and also tested the as-prepared materials as anodes for lithium-ion batteries combined with CMC and PVDF binders. Results demonstrated that the as-obtained CuO-carbon composite had much better

electrochemical properties, especially after long cycling, when using CMC as the binder. This can be attributed to the conductive carbon, the appropriate binder selection, and also the increase in the specific surface area of the material. The successful introduction of carbon into CuO spheres can enhance the electronic conductivity both between and within the CuO particles; the CMC binder could provide good internal binding of the material so that it can survive the large repeated dimensional changes of the electrode during charge and discharge. Additionally, the carbon coating process changes the morphology and increases the specific surface area of the material. This simple and efficient carbon coating method could also be extended to other metal oxides.

CHAPTER 6 HIGH CAPACITY FLEXIBLE FREE-STANDING GRAPHENE-SILICON COMPOSITE FILM FOR LITHIUM-ION BATTERIES

6. 1 Introduction

Recently, there has been strong market demand for ultra-thin, flexible energy storage devices to meet the various design and power needs of soft portable electronic equipment, such as roll-up displays and wearable devices. Active radio-frequency identification tags and integrated circuit smart cards also require flexible or bendable batteries for durability in everyday use [88]. The design of such soft electrochemical devices requires the development of freestanding flexible and robust electrode materials.

Carbon-based materials have shown favourable flexibility and hence, are promising for producing flexible and bendable free-standing electrodes [89, 90, 91]. Carbon-based paper-like flexible materials for batteries and supercapacitors have been extensively studied [92, 93, 94]. The paper-like carbon-based materials, such as carbon nanotube and graphene electrode materials, are lightweight, flexible and have good cycling stability, however, the capacities are just about 100-200 mAh g^{-1} [95, 96]. In order to improve the practical capacity of the free-standing electrode materials, an electrochemically active second phase with higher capacity can be incorporated into the carbon-based paper-like films [97].

Silicon is the most attractive anode material for lithium batteries because it has a low discharge potential and the highest known theoretical charge capacity of about 4,200 mAh g^{-1}, corresponding to the fully lithiated composition of $Li_{4.4}Si$ [98], which is more than ten times higher than for commercial graphite anode (372 mA g^{-1}) [99]. Therefore, Si is a good candidate for use as a second electrochemically active phase to incorporate into the carbon-based free-standing electrode. However, silicon-based electrodes suffer from poor cycling stability due to silicon's volume changes by 400% upon insertion and extraction of lithium [100], leading to cracking and crumbling of the electrode, which results in the failure of the anode in a few cycles. The current strategies to overcome the so-called pulverization of Si are focused on using composite materials [101, 102]. Nanosize silicon can be homogeneously dispersed within suitable carbon materials, resulting in a nanocomposite, in which the carbon materials act as a buffering matrix to accommodate the large volume change upon cycling [103, 104]. Therefore, we designed free-standing graphene-Si composite materials based on following ideas:

(a) Adding high capacity Si into film-like graphene electrode can improve the capacity of the free-standing graphene electrode.
(b) The cycling stability of Si will be improved by embedding it into graphene nanosheets.

Here, we report, for the first time, to the best of our knowledge, using construction of a soft and flexible free-standing carbon matrix to improve the performance of Si anode for lithium-ion battery application. On the other hand, the methodology for

preparation of this paper-like thin film material can be extended to other flexible free-standing inorganic-carbon materials for various applications.

6. 2 Experimental

6.2.1 Synthesis of graphite oxide

Graphite oxide (GO) was synthesized from natural graphite powder (Fluka) by a modified Hummers method [105, 106]. Graphite powder (3 g) was put into an 80 °C solution of concentrated H_2SO_4 (12 mL), $K_2S_2O_8$ (2.5 g), and P_2O_5 (2.5 g). The mixture was kept at 80 °C for 5 h and then diluted with 0.5 L of de-ionized (DI) water and left overnight. Then, the mixture was filtered and washed with DI water and dried naturally overnight. It was then put into 0 °C concentrated H_2SO_4 (120 mL), and $KMnO_4$ (15 g) was gradually added under stirring, with the temperature of the mixture kept below 20 °C by cooling. The mixture was then stirred at 35 °C for 2 h and diluted with DI water (250 mL) in an ice bath to keep the temperature below 50 °C. After that, the mixture was stirred for 2 h, and then an additional 0.7 L of DI water was added. Shortly afterwards, 20 mL of 30% H_2O_2 was added to the mixture, which was then filtered and washed with a 1:10 HCl aqueous solution (1 L) to remove metal ions, followed by 1 L of DI water to remove the acid.

6.2.2 Preparation of graphene and graphene-Si composite films

To prepare graphene film, 100 mg (0.5 mmol) of NaOH and 145 mg (0.1 mmol) of pyrenebutyric acid were put into 100 mL (0.1 mg mL^{-1}) of GO dispersion. Hydrazine monohydrate (500 μL, 2 mmol) was then added into the solution. After that, the

mixture was reduced at 80 ^{o}C for 24 h. A poly(vinylidene) fluoride (PVDF) membrane (pore size 0.22 μm, GV Millipore) was wetted in a 50:50 v/v DI water to ethanol solution for 30 minutes. Passing the as-prepared graphene suspension through the wetted PVDF filter in a filtration cell (Whatman 47mm) under a positive pressure of 400 kPa then produced a free-standing mat of graphene. Subsequently, the resultant graphene mat was washed with 200 ml of DI water and then peeled off from the PVDF filter after drying overnight in a vacuum oven. Finally, the as-prepared films were heat-treated at 500 °C in argon atmosphere to remove -H and -OH groups.

Figure 6.1 Schematic diagram of the composite film fabrication.

To prepare the graphene-Si composite paper, a dispersion of graphene-Si was prepared by an in situ method. Simply add 10 mg nano-silicon powder into the GO dispersion together with the same amount of NaOH and hydrazine monohydrate, followed by 2 h ultrasonication. Then, the same procedures as were applied in the fabrication of graphene film were repeated to produce the composite film of graphene-Si (see Figure 6.1).

6.2.3 Structural and Electrochemical Characterization

Graphene, graphene-Si papers, and Si powder were characterised by X-ray diffraction (XRD) on a GBC MMA 017 diffractometer with Cu Kα radiation. Raman spectroscopy were conducted to further confirm the preparation of free-standing graphene and graphene-Si films using a JOBIN YVON HR800 confocal Raman system with 632.8 nm diode laser excitation on a 300 lines/mm grating at room temperature. Morphologies of the free-standing graphene and graphene-Si were examined using scanning electron microscopy (SEM; JEOL JEM-3000, 30 kV) and field emission SEM (FE-SEM; JEOL JSM-7500FA). Thermogravimetric analysis (TGA) was performed using a Mettler Toledo TGA/DSC 1 STAR System to examine the graphene and Si contents.

The as-prepared free-standing graphene and graphene-Si composite films were used to fabricate the electrodes, using CR 2032 coin-type cells, which were assembled in an Ar-filled glove box (Mbraun, Unilab, Germany) by stacking the anodes with a porous polypropylene separator and a lithium foil counter and reference electrode.

The electrolyte used was 1 M $LiPF_6$ in a 50:50 (v/v) mixture of ethylene carbonate (EC) and dimethyl carbonate (DMC). The cells were galvanostatically discharged and charged within a voltage window of 0.02-1.2 V (vs. Li/Li^+) at a current density of 50 mA g^{-1} and a temperature of 20 ^oC. The discharge capacities are based on the total amount of active material in the electrodes.

6. 3 Results and Discussion

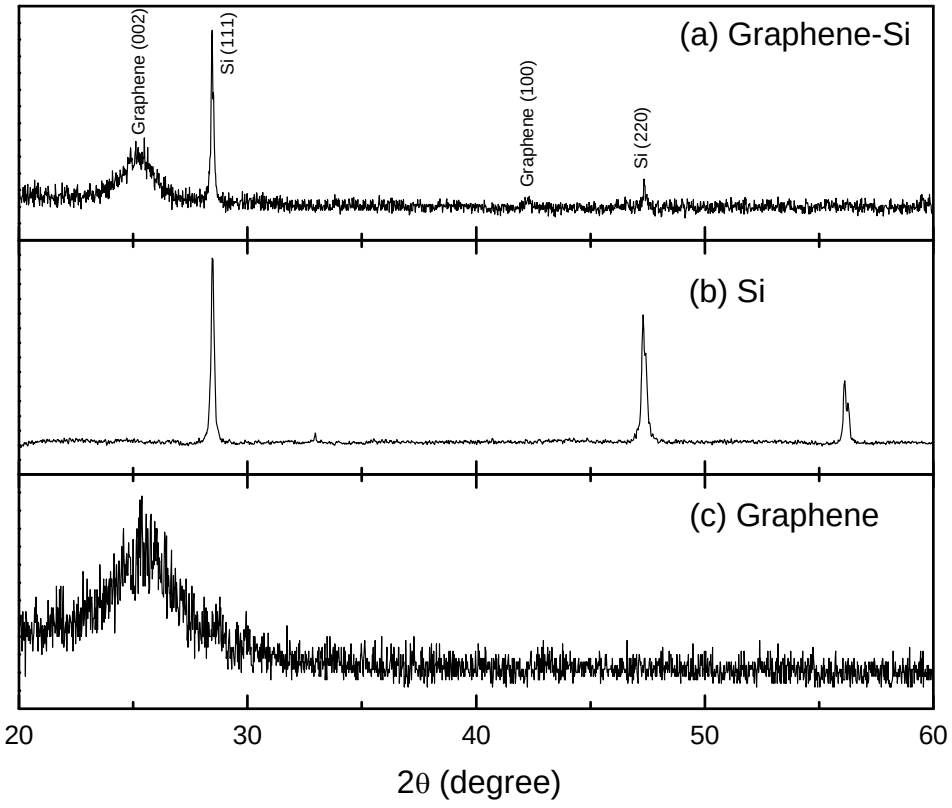

Figure 6.2 X-ray diffraction patterns for free-standing graphene-Si film (a), Si nanopowder (b), and free-standing graphene film (c).

X-ray diffraction and Raman spectroscopy were conducted to confirm that the graphene-Si composite was obtained through in-situ reduction of the mixed suspension of graphene oxide and Si powder. The XRD pattern of the graphene-Si composite paper displays two major peaks of Si (28.43° and 47.60°) [107] and two peaks of graphene (25.54° and 42.91°) [108] (Figure 6.2). Figure 6.3 presents the Raman spectrum of graphene-Si composite paper, where the Raman spectrum of Si nanopowder and pure graphene paper are also plotted for comparison. The Raman spectrum of graphene-Si composite displays a main peak at around 510 cm^{-1}, which is due to the Si particles [109] , and another two peaks at around 1355 cm^{-1} and 1597 cm^{-1}, which are identified as the D band and the G band of graphene [110]. This indicates that the graphene-Si composite was successfully synthesised via an in-situ chemical method from graphite oxide and Si powder precursors.

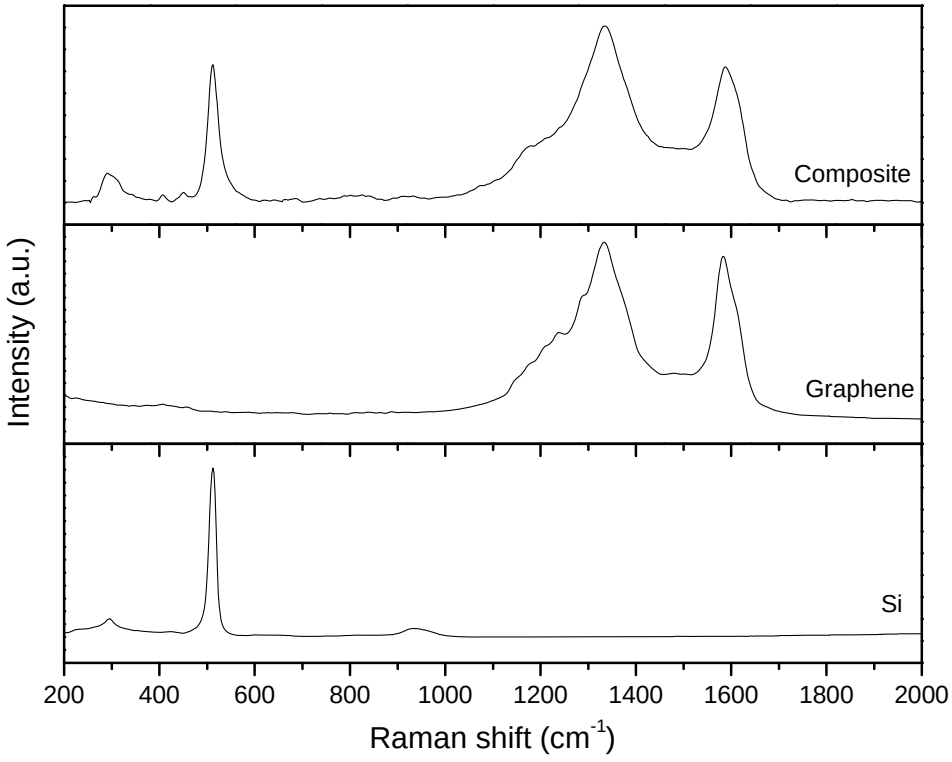

Figure 6.3 Raman spectra for free-standing graphene-Si composite film, graphene film, and Si nanopowder.

Figure 6.4(a) presents a FESEM image of the graphene film from the top view, showing well packed layered platelets composed of cured nanosheets. Such sheets are at times folded or continuous, and it is possible to distinguish the edges of individual sheets, including kinked and wrinkled areas. Figure 6.4(b) shows a planar-view FESEM image of the free-standing graphene-Si film. Both the edges of the graphene and the nanosize of the Si are clearly observed. Si nanoparticles with a diameter of 20–80 nm are spread over the graphene sheet surface. A cross-sectional image of a free-standing graphene-Si film is shown in Figure 6.4(c); the thickness is about 10 μm, and pockets of void space are clearly visible. The Si particles are embedded uniformly into the layers of graphene sheets (Figure 6.4(d)). The pure free-standing graphene electrode also presents pockets of void space (see Figure 6.4(a) inset). The TEM image shows that the Si nanoparticles are wrapped up in the multiple overlapping layers of graphene nanosheets (Figure 6.4(e)). Results of FESEM examination combined with EDS mapping for the elements C and Si are shown in Figure 6.4(f). The bright regions correspond to the presence of the elements C and Si, respectively, and indicate that C and Si are distributed uniformly throughout the whole area. The uniform distribution of Si nanoparticles among the graphene is due to the in-situ synthesis method used for preparation of the free-standing electrode, as mentioned in the experimental part.

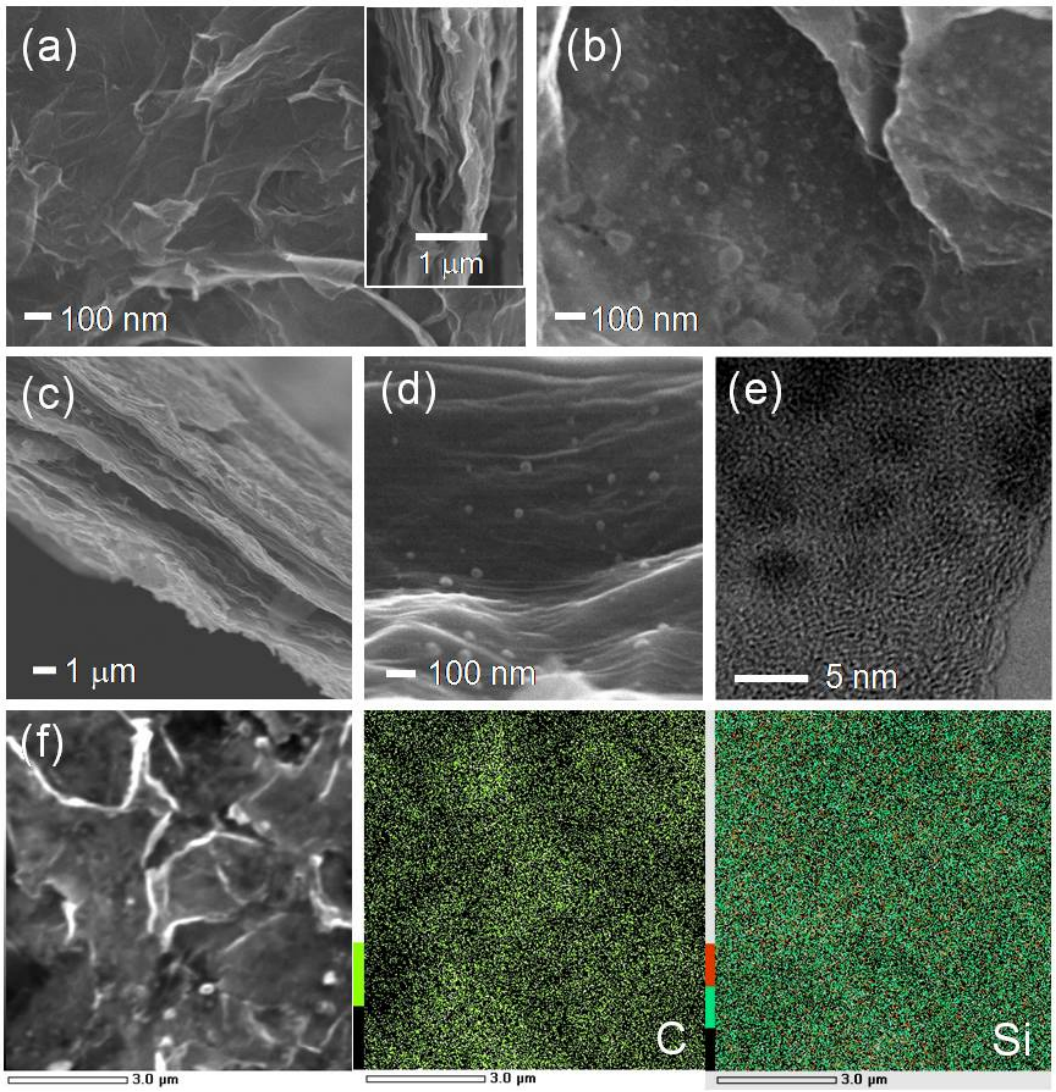

Figure 6.4 FESEM images: top view of free-standing graphene film (a) with a cross-sectional view (inset), free-standing graphene-Si composite film (b), and cross-sectional views of the composite film at low (c) and high (d) magnification; TEM image of graphene-Si composite (e); FESEM image of graphene-Si (f), with corresponding EDS mapping of carbon and silicon.

For quantifying the amount of Si in the graphene-Si film materials, TGA was carried out in air. The samples were heated from 50 to 800 °C at a rate of 5 °C min^{-1}. Figure 6.5 shows the TGA curves of the graphene-Si sample along with those of the nanocrystalline Si powders and bare graphene paper. As can be seen from Figure 6.5,

the graphene-Si paper materials show rapid mass loss between 350 and 600 °C. As the nanocrystalline Si powder remains stable in this temperature range, any weight change corresponds to the oxidation of graphene. Therefore, the change in weight before and after the oxidation of graphene directly translates into the amount of graphene in the graphene-Si paper materials. With the use of this method, it was estimated that the amount of graphene in the composites was 73.6 wt %. Therefore the Si content in the composite paper is 26.4%.

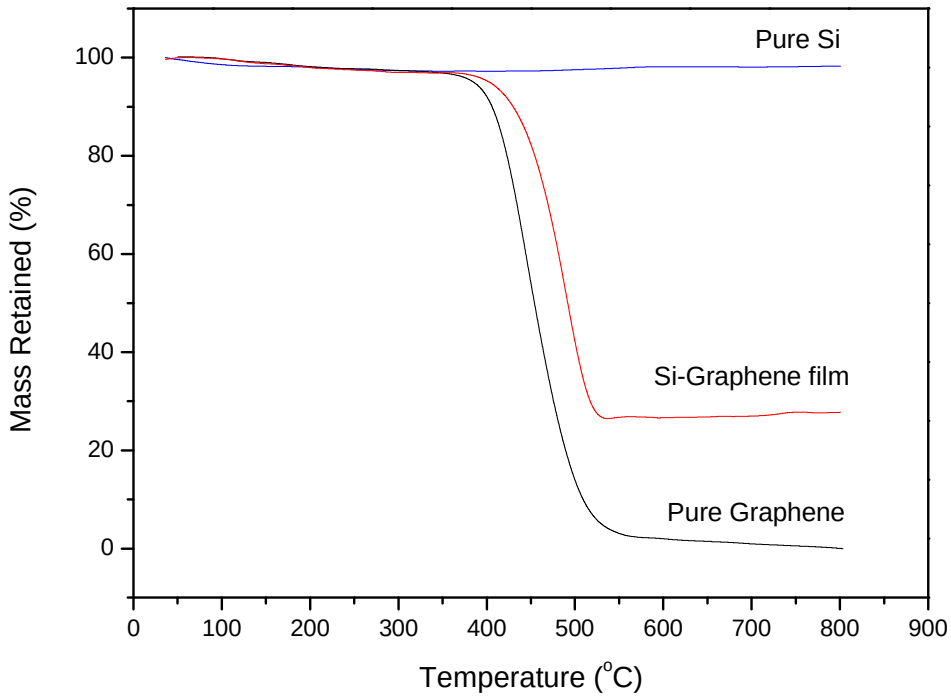

Figure 6.5 TGA curves of graphene-Si composite film, graphene film, and Si nanopowder.

Figure 3 shows discharge capacity versus cycle number for cells made from free-standing graphene and graphene-Si composite film electrodes. It can be seen that the capacity of the pure graphene film electrode is about 304 mAh g^{-1}. The Li storage

capacity of the free-standing graphene is lower than that of the conventional graphene electrode which is attributed to the lower conductivity of the free-standing electrode compared to the conventional electrode. By adding a second electrochemically active phase, Si nanoparticles, the capacity of the composite material is significantly improved to about 708 mAh g^{-1}, even after 100 cycles. On the other hand, the cycling performance of Si in the graphene composite is much better than that of pure Si electrode. Our previous results showed that pristine nanosize Si electrode has an initial discharge capacity of 3026 mAh g^{-1}, with a coulombic efficiency of 58%. The capacity drops rapidly to 346 mAh g^{-1} after 30 cycles [111]. Interestingly, the free-standing graphene-Si electrode gives a reversible capacity of 708 mAh g^{-1} without obvious capacity loss over 100 cycles. It is well known that conventional silicon-based electrodes suffer from poor cycling stability due to silicon's volume changes by 400% upon insertion and extraction of lithium, leading to cracking and crumbling of the electrode, which results in the failure of the anode within a few cycles [100,112]. In the case of the free-standing graphene-Si composite electrode, nanosize Si particles are homogeneously distributed between the graphene sheets. The graphene serves not only for dilution, to prevent Si particles from aggregating, but also as an efficient elastic matrix to accommodate the mechanical stresses/strains experienced by the Si phase, thus maintaining the structural integrity of the composite electrode during the alloying/de-alloying processes [113,114]. Even though the volume expansion still occurs, the electrode is not pulverized, since graphene-Si has enough void spaces to buffer the volume change. The excellent electron and ion transfer kinetics associated with graphene also contributes to the superior electrochemical performance of the graphene-Si composite by lowering the internal resistance for both electrons and lithium ions to

facilitate the dealloying reaction over the small surface area of the silicon particles. On the other hand, the specially designed free-standing film materials, integrating the active materials and the current collector into the one flexible film, can prevent loss of the electrical contact between active materials and substrate, which normally occurs for the conventional electrode [115]. The charge and discharge curves of the first and second cycles are shown in the Figure 3 (inset). The large irreversible capacity observed in the first cycle may be caused by the formation of the solid electrolyte interphase. It may also occur because of the large amount of graphene used in the composite. It has been reported that graphene anode showed large irreversible capacity for the first cycle, which is associated with the formation of a SEI layer [21].

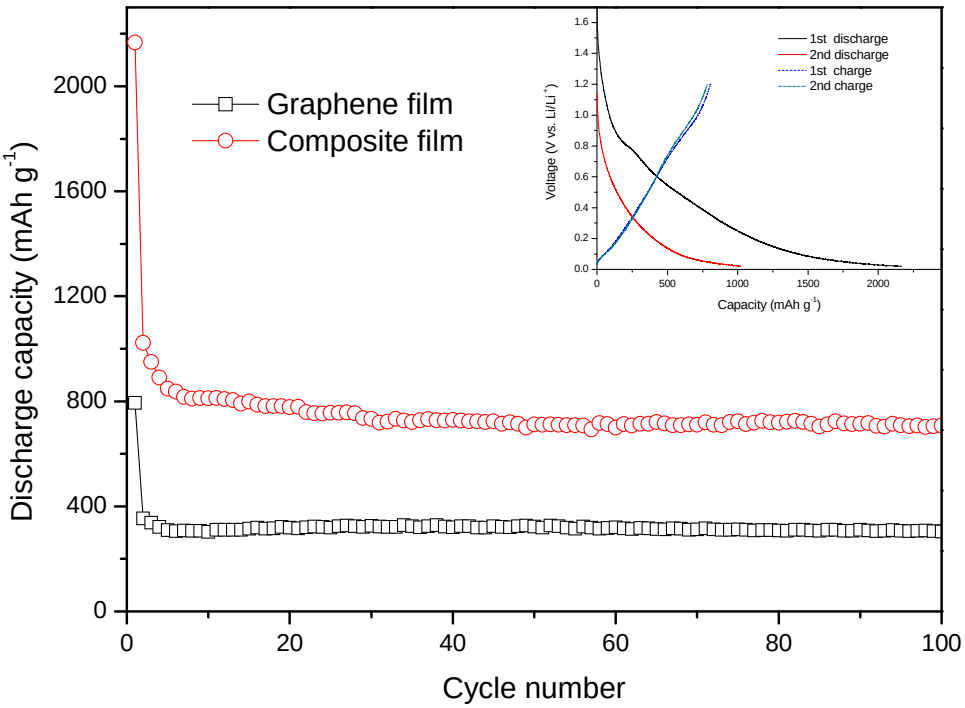

Figure 6.6 Discharge capacity vs. cycle number for the electrodes made from graphene film and graphene-Si composite film.

6. 4 Chapter Summary

In this chapter, a free-standing graphene-Si composite film was synthesized, based on the idea of adding high capacity nanoparticle Si into graphene electrode to improve the capacity of the free-standing, film-like, graphene electrode. A reversible discharge capacity of 708 mAh g^{-1} for the as-obtained composite material was achieved, even after 100 cycles. The preliminary results demonstrate good prospects for the combination of graphene with a second high-capacity, electrochemically active phase to improve the total capacity of the electrode. On the other hand, the methodology for the preparation of this film-like material can be extended to other flexible, free-standing, inorganic-carbon materials for various applications.

CHAPTER 7 HYDROTHERMAL SYNTHESIS OF NANOSTRUCTURED MANGANESE DIOXIDE UNDER MAGNETIC FIELD FOR RECHARGEABLE LITHIUM BATTERIES

7. 1 Introduction

Manganese oxides have porous structures and can be used as cathode materials for lithium batteries [81, 116]. Nanostructured manganese oxides have demonstrated enhanced electrochemical properties compared to their bulk counterparts [117, 118, 119]. It is well-known that cathodes with high surface area show better discharge performance and lower degradation rates than cathodes having lower surface areas [120]. Therefore, better electrochemical performance can be expected by adopting various synthesis conditions which can yield high surface area nanostructured materials with different morphologies.

Nanostructured manganese oxides can be prepared through various methods, such as combining the template-based method and sol-gel chemistry [118], the facile wet chemical method [121], and the hydrothermal method [122]. Hydrothermal synthesis has been an interesting technique to prepare materials with different nano-architectures, such as nanowires, nanorods, nanobelts, nanoflowers, and so forth [123, 124, 125]. The main advantage of the hydrothermal technique over other soft chemical routes is the ability to control the nanostructures by properly choosing the reaction temperature, time, solvent, and concentrations without any major structure-directing agents or templates. The effects of temperature, time, solvent, and

concentration on the morphologies of powders prepared by the hydrothermal method have been extensively studied and reported [125, 126, 127]. However, study of the effects of pulsed magnetic field on the morphologies of the resultant powders during hydrothermal synthesis is a new exploration. This is the motivation behind the present work on the synthesis of nanostructured MnO_2 using the hydrothermal method under pulsed magnetic field. The possibility of using this MnO_2 material as cathode for rechargeable lithium batteries is also examined.

7. 2 Experimental

7.2.1 Synthesis of Nanostructured MnO_2

Manganese dioxide (MnO_2) powder was synthesized by the redox hydrothermal method with or without different pulsed magnetic fields. The chemical reaction between $MnSO_4$ and $(NH_4)_2S_2O_8$ is as follows:

$$MnSO_4 + (NH_4)_2S_2O_8 + 2H_2O \rightarrow MnO_2 + (NH_4)_2SO_4 + 2H_2SO_4 \quad (7.1)$$

All chemical reagents in this work were analytical grade. In a general experiment, 1.082 g (6.4 mmol) manganese sulfate monohydrate ($MnSO_4 \cdot H_2O$) and 1.461 g (6.4 mmol) ammonium persulfate ($(NH_4)_2S_2O_8$) were put into 20 ml distilled water at room temperature to form a homogeneous solution, which was then transferred into a 25 ml Teflon-lined stainless steel autoclave, filling it up to 80% of the whole volume. The sealed solution was kept at 150 °C for 8 hours. During this time, different intensities of pulsed magnetic fields (0 T, 2 T, and 4 T) were applied respectively. After the autoclave was cooled down to room temperature naturally, the obtained

products were then filtered and washed with distilled water to remove the remaining ions. Finally, the as-prepared materials were dried in a vacuum oven at 80 °C overnight.

7.2.2 Physical and Electrochemical Characterization

X-ray diffraction (XRD) results were obtained using a GBC-MMA-017 X-ray diffractometer with Cu Kα radiation (λ = 1.5418 Å). The morphology of samples was investigated by field emission scanning electron microscopy (FE-SEM, JEOL JSM-7500F) and transmission electron microscopy (TEM, JEOL-2011, 200 kV). Energy-dispersive X-ray (EDX) spectroscopy was used for elemental analysis of the materials.

To fabricate the MnO_2 electrodes, 70 wt% MnO_2 powder was mixed with 20 wt% carbon black and 10 wt% carboxymethyl cellulose (CMC) binder. De-ionized water was used as the dispersant to form the slurries. The electrochemical characterizations were carried out using CR 2032 coin-type cells, which were assembled in an Ar-filled glove box (Mbraun, Unilab, Germany) by stacking a porous polypropylene separator and a lithium foil counter electrode. The electrolyte used was 1 M $LiPF_6$ in a 50:50 (v/v) mixture of ethylene carbonate (EC) and dimethyl carbonate (DMC). The cells were galvanostatically discharged and charged within a voltage window of 2.0 - 4.0 V (vs. Li/Li^+) at a current density of 50 mA g^{-1} and a temperature of 20 °C. The discharge capacities are based on the amount of active material in the electrodes.

7. 3 Results and discussion

7.3.1 Physical and Structural Characterization

Figure 7.1 shows the XRD patterns of the MnO_2 materials obtained at 150 °C with (4 T) and without magnetic field. All the diffraction peaks correspond well with standard crystallographic data and can be indexed primarily to the pure tetragonal structure of β-MnO_2 (JCPDS card 00-024-0735), but very tiny peaks also correspond to γ-MnO_2 (JCPDS card 00-014-0644) and α-MnO_2 (JCPDS card 00-044-0141).

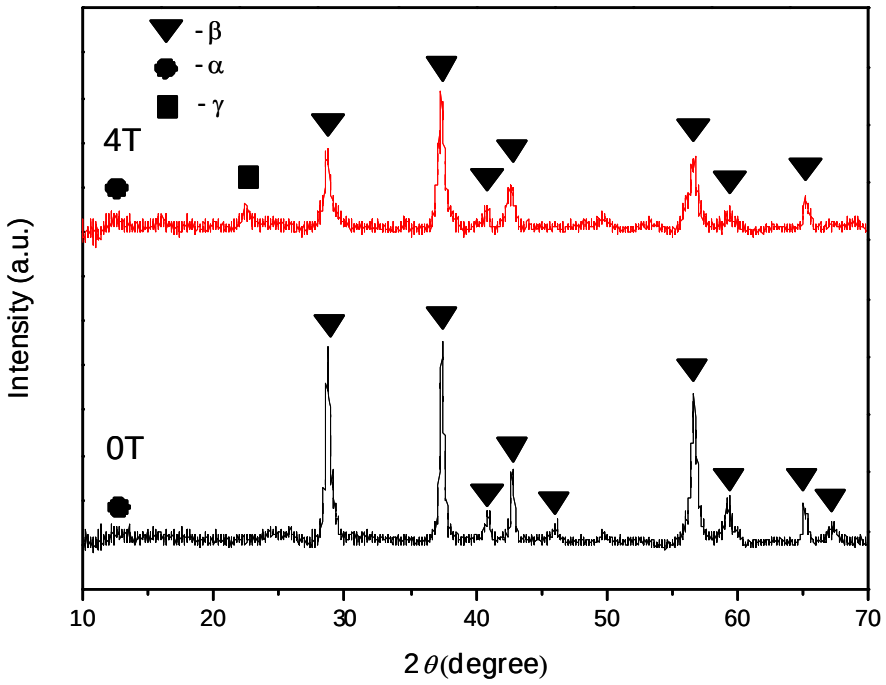

Figure 7.1 XRD pattern of the MnO_2 obtained without and with a 4 T magnetic field.

Figure 7.2(a), (b), and (c) are FE-SEM images of the MnO_2 powders synthesized with no magnetic field and with 2 T and 4 T pulsed magnetic fields. Comparing the three images, it can be easily seen that the as-prepared MnO_2 without magnetic field exhibits urchin-like structures which consist of nanofibres about 1 μm in length (Figure 7.2(a)); after using 2 T and 4 T pulsed magnetic fields, the morphology of the

MnO_2 changes to rambutan-like structures with longer nanofibres (Figure 7.2(b) and (c)). From observation of the images we can estimate that the nanofibres for the MnO_2 obtained at 2 T are approximately 2 μm long. In the material synthesized under a 4 T magnetic field, the nanofibres are even longer than 3 μm. Figure 7.2(d) and (e) are the EDX spectroscopy results for the as-prepared materials obtained at 0 T and 4 T magnetic fields. They show that MnO_2 was the only product, which is consistent with the XRD patterns. The peaks in the region labelled C are from the conductive adhesive.

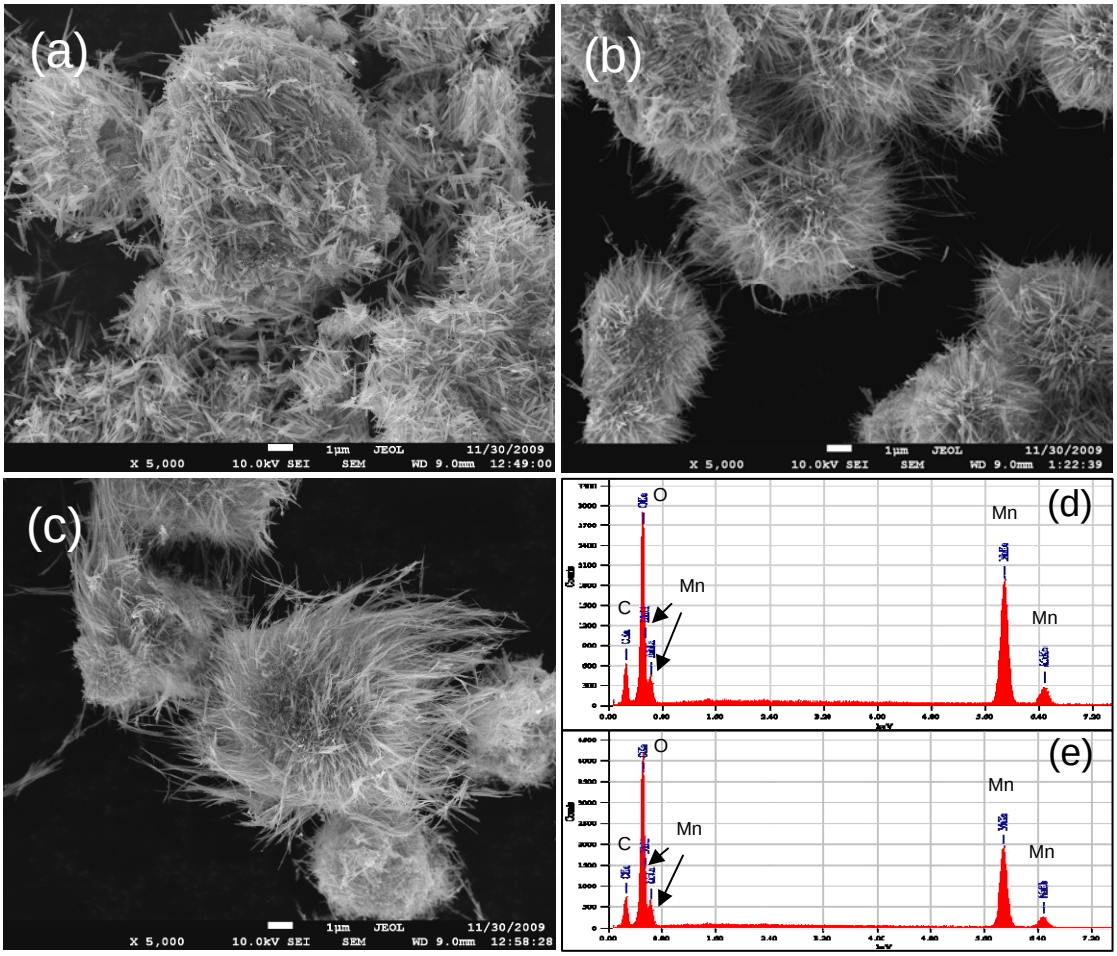

Figure 7.2 SEM images (a), (b), and (c) for the MnO_2 obtained without magnetic field, and with 2 T and 4 T fields, respectively; EDX results for the MnO_2 obtained (d) without magnetic field and (e) with a 4 T field.

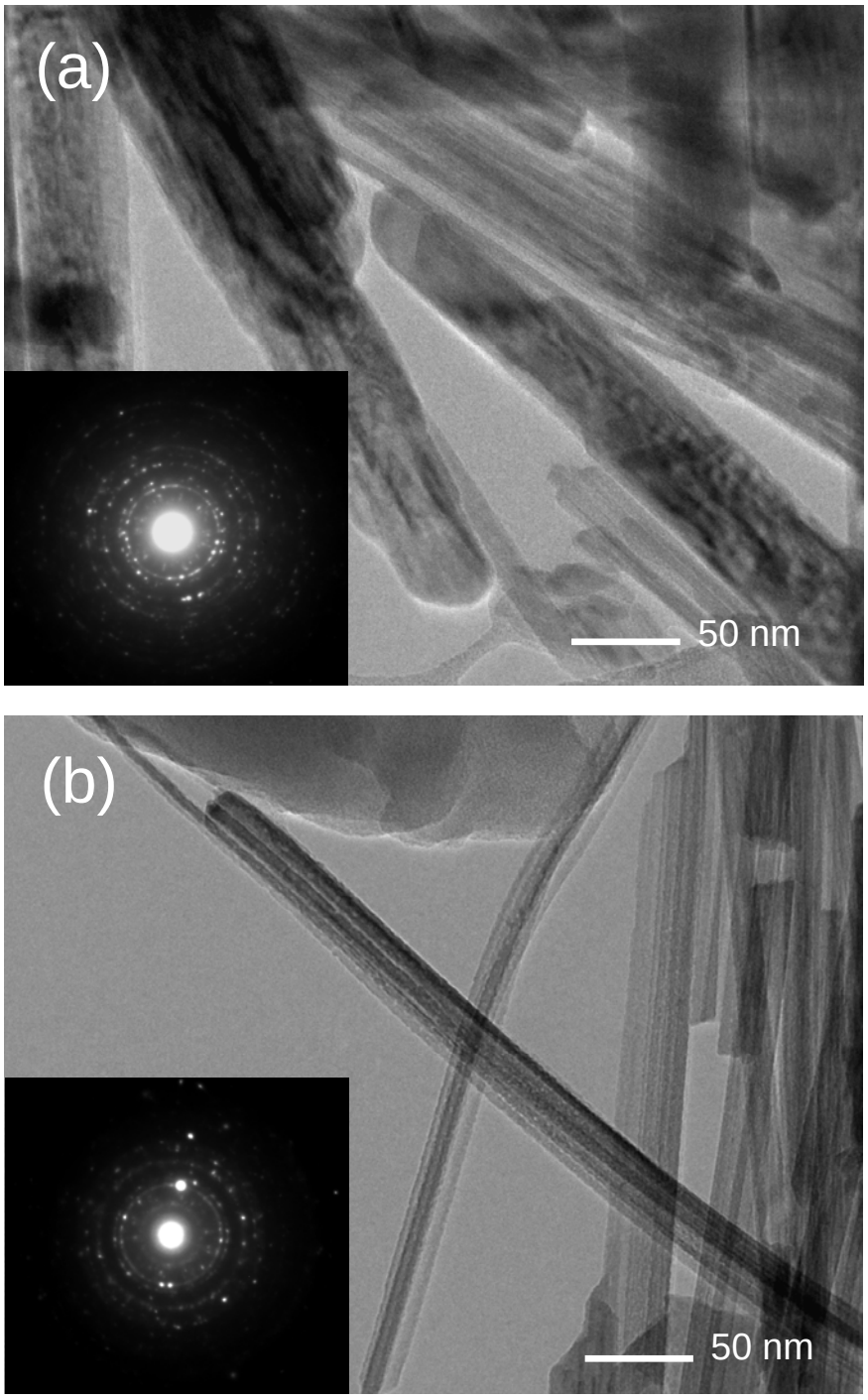

Figure 7.3 TEM images and SAED patterns (inset) of the MnO_2 obtained (a) without magnetic field and (b) with a 4 T field.

Figure 7.3 contains TEM images of the as-prepared MnO_2 materials obtained in 0 T and 4 T magnetic fields. It can be seen that the diameter of the nanofibres prepared with a 4 T magnetic field (10-20 nm) is much smaller than for the sample obtained without magnetic field (40-50 nm). The selected-area electron diffraction (SAED) patterns (inset) display several concentric electron diffraction rings and some regular highlighted diffraction spots on the rings which can be indexed to β-MnO_2. These results also agree very well with the XRD analysis. The possible reason for the magnetic field effect on the materials is that the magnetic field provides a special directional environment during the hydrothermal process, which affects the nanoparticle nucleation and growth. Thus, the crystals of the MnO_2 materials follow the magnetic field direction and form narrower and longer fibres. To further study the magnetic field effects on the materials, Brunauer-Emmett-Teller (BET) tests were also performed. The results made it clear that an increase in the intensity of the pulsed magnetic field produced a pronounced increase in the BET specific surface area, S_{BET}. The powders obtained from the 2 T and 4 T pulsed magnetic fields exhibit the remarkably high S_{BET} values of 40.27 and 46.18 $m^2\ g^{-1}$, respectively, while the sample prepared without magnetic field has a value of only 23.65 $m^2\ g^{-1}$.

7.3.2 Electrochemical Properties

Cyclic voltammograms of the MnO_2 materials synthesized without magnetic field and with a 4 T pulsed magnetic field at a scan rate of 0.1 mV s^{-1} at 20 °C are shown in Figure 7.4. During the cathodic and anodic scanning processes, an oxidation potential peak (E_O) and a reduction potential peak (E_R) were observed. It can be easily seen that the peak intensities are higher for the sample of MnO_2 prepared under the 4 T pulsed magnetic field than for the sample of MnO_2 prepared without

magnetic field, which demonstrates that the 4 T synthesized MnO_2 material has higher reactivity in the lithium cells due to the larger BET specific surface area.

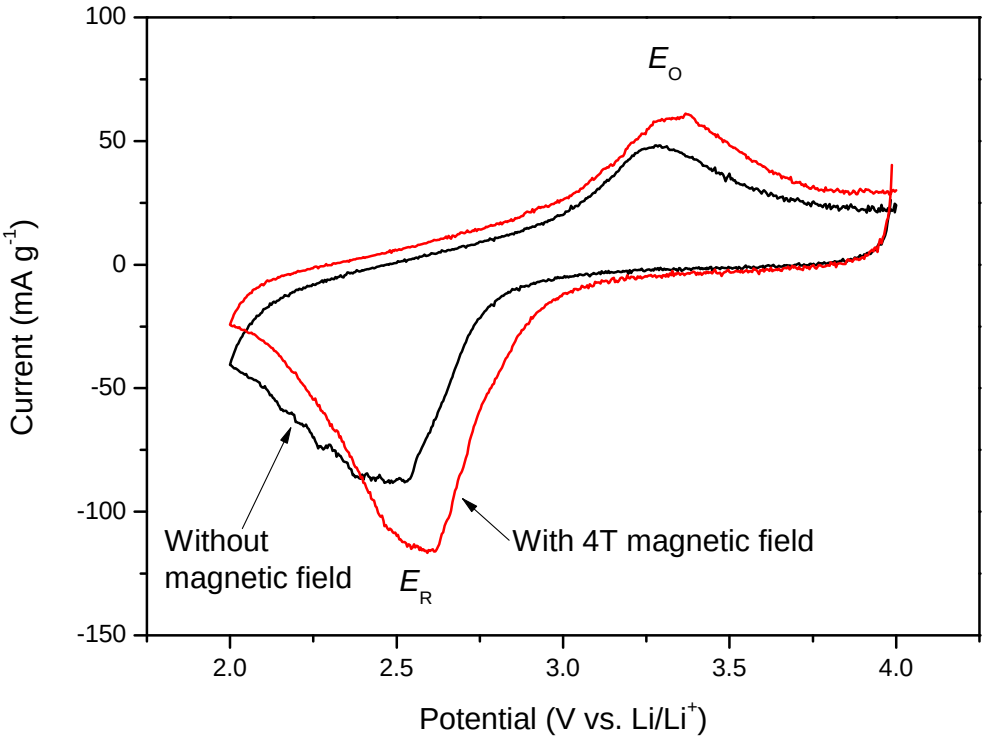

Figure 7.4 Cyclic voltammograms for the MnO_2 materials synthesized with and without magnetic field.

Figure 7.5(a) presents the first two typical discharge and charge curves for MnO_2 materials prepared under different magnetic fields. Comparing the first discharge and charge capacities of the MnO_2 electrodes synthesized without magnetic field with those synthesized with 2 T and 4 T pulsed magnetic fields, it can be found that the irreversible capacity loss for the first cycle is about 27.6% (0 T), 9.8% (2 T), and 2.1% (4 T), respectively. These results show that applying pulsed magnetic fields can greatly help to improve the electrochemical properties of MnO_2.

Figure 7.5(b) shows the discharge capacity versus cycle number for cells made with MnO_2 electrodes synthesized with and without magnetic fields. It can be observed that the capacity of the electrodes made with MnO_2 materials synthesized under 4 T pulsed magnetic field (121.8 mAh g^{-1}) is improved compared to the MnO_2 synthesized without magnetic field (103.0 mAh g^{-1}) after 30 cycles. Furthermore, the MnO_2 synthesized under 4 T pulsed magnetic field gives a better capacity retention of about 64.5% compared to results for the 0 T and 2 T materials, which are 50.7% and 54.2%, respectively, beyond 30 cycles. We may conclude that these improvements are due to the special morphologies and the increase in the BET surface areas of the materials. The reactivity of MnO_2 electrodes with lithium is improved when the samples have larger BET surface areas, as has been reported by Xia's group [128].

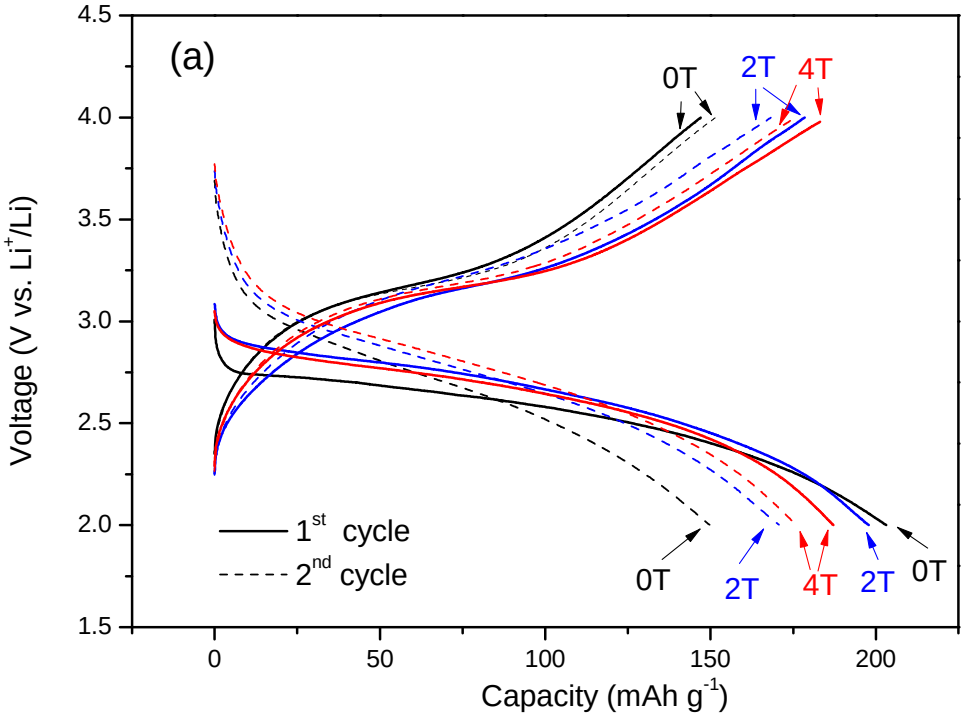

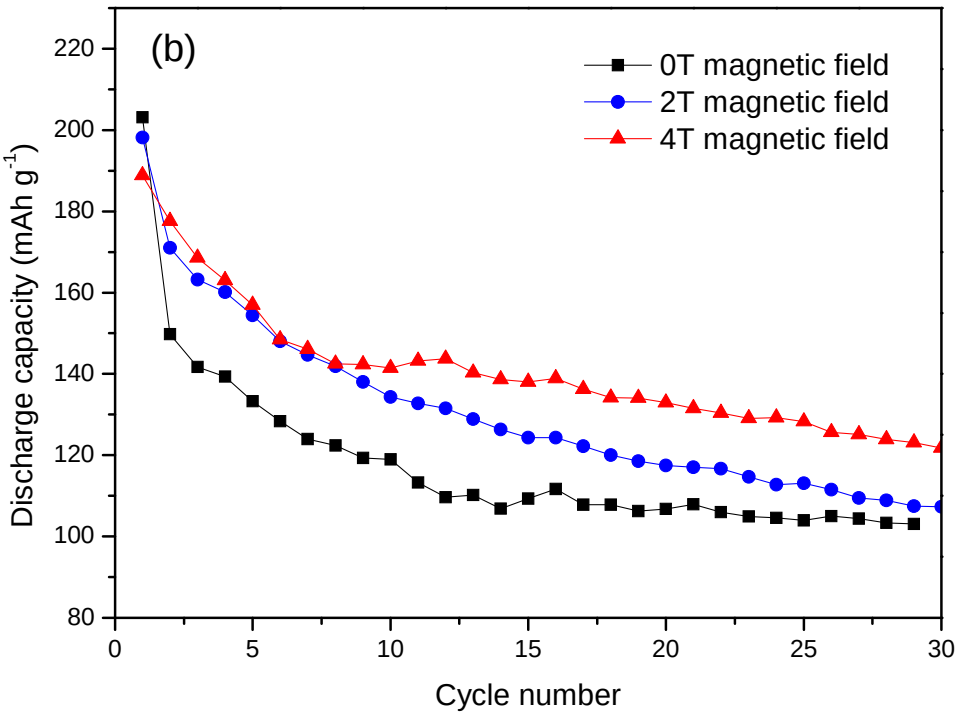

Figure 7.5 (a) Discharge and charge curves for the MnO_2 materials prepared with different magnetic fields. (b) Discharge capacities vs. cycle number for the as-prepared MnO_2.

7. 4 Chapter Summary

Nanostructured MnO_2 powders were synthesized by the hydrothermal method under different pulsed magnetic fields, and studied physically and electrochemically in this chapter. It was found that magnetic fields have obvious effects on the morphologies of MnO_2 materials. The morphology of the MnO_2 prepared without magnetic field has an urchin-like structure, while the MnO_2 prepared with magnetic fields has a rambutan-like structure. A pronounced increase in the Brunauer-Emmett-Teller (BET) specific surface area was obtained when the intensities of the pulsed magnetic

fields increased ($S_{BET,0T} < S_{BET,2T} < S_{BET,4T}$). The electrochemistry results also show that the electrochemical performance of the MnO_2 materials was improved with increasing BET surface area. The MnO_2 prepared under a magnetic field of 4 T shows a capacity of 121.8 mAh g^{-1}, while the MnO_2 prepared without magnetic field only shows 103.0 mAh g^{-1} after 30 cycles.

CHAPTER 8 CONCLUSIONS

In this Master's study, several anode and cathode materials were synthesized and investigated for use in rechargeable lithium-ion batteries, by means of different synthesis method and characterization techniques.

The anode electrode materials were systematically reviewed. Transition metal oxides, NiO and bare/carbon coated CuO, were investigated for use as anode materials. A novel free-standing graphene-Si composite film was also studied for the first time. Research into the cathode materials was mainly focused on a series of MnO_2 materials produced by a magnetic field assisted hydrothermal method. Furthermore, a new type of environmentally friendly binder, CMC, was also examined for use in combination with transition metal oxides for application in rechargeable lithium-ion batteries.

In this study, spray pyrolysis synthesized transition metal oxides, NiO and bare/carbon coated CuO hollow spheres, were investigated as anode materials in rechargeable lithium-ion batteries. When fabricating electrodes, different binders (PVDF and CMC) were used in conjunction with the as-obtained transition metal oxides. The as-selected CMC binder and the carbon coating method made great contributions to the electrochemical performances of the materials, especially in cycling performance. What is more important, the findings on non-toxic and water soluble CMC binder, and the simple one-step and large-scale spray pyrolysis method

are directly relevant for industrial application. Further study can be focused on the effects of different amounts of carbon precursor in the materials.

The preparation of graphene-Si composite film using a filtration technique was also introduced for the production of a novel free-standing anode electrode for rechargeable lithium-ion batteries. The results demonstrated the active support that Si nanoparticles gave to graphene nanosheets in electrochemical performance. On the other hand, the methodology of preparation of this paper-like thin film material can be extended to other flexible free-standing inorganic-carbon materials for various applications.

An investigation of the synthesis of nanostructured MnO_2 for cathode using a magnetic field assisted hydrothermal method was conducted. Magnetic fields had obvious effects on the morphologies of the MnO_2 materials. The Brunauer-Emmett-Teller (BET) surface areas of the MnO_2 materials were increased when the intensity of the magnetic field increased. The electrochemistry results showed that the electrochemical performance of the MnO_2 materials was improved with increasing BET surface area.

REFERENCES

[1] Winter M, Brodd RJ, (2004) Chem Rev, 104:4245.

[2] David L, Thomas BR, (2002) Handbook of Batteries, 3rd Edition, New York, London: McGraw-Hill.

[3] Tarascon JM, Armand M, (2001) Nature, 414:359.

[4] Dell RM, Rand DAJ, (2001) Understanding Batteries, 1st Edition, RSC paperbacks, Cambridge: Royal Society of Chemistry, P264.

[5] Asimov I, (1982) Asimov's Biographical Encyclopedia of Science and Technology, Garden City: Doubleday & Company, P941.

[6] Buchmann I, (2001) Batteries in A Portable World: A Handbook on Rechargeable Batteries for Non-engineers, 2nd Edition, New York: Cadex Electronics Inc, P292.

[7] Owen JR, (1997) Chem Soc Rev, 26:259.

[8] Winter M, Besenhard JO, Spahr ME, Novak P, (1998) Adv Mater, 10:725.

[9] Hardwick LJ, (2007) PhD Thesis, Switzerland: Paul Scherrer Institute.

[10] Nishi Y, (2001) Chem Record, 1:406.

[11] Yamamura J, Ozaki Y, Morita A, Ohta A, (1993) J Power Sources 43:233.

[12] Mabuchi A, (1994) Tanso, 165:298.

[13] Dahn JR, Zheng T, Liu YH, Xue JS, (1995) Science, 270:590.

[14] Azuma H, Imoto H, Yamada S, Sekai K, (1999) J Power Sources, 81:1.

[15] Tirado JL, (2003) Mater Sci Eng R, 40:103.

[16] Novoselov KS, Geim AK, Morozov SV, Jiang D, Zhang Y, Dubonos SV, (2004) Science, 306:666.

[17] Novoselov KS, Geim AK, Morozov SV, Jiang D, Katsnelson MI, Grigorieva IV, (2005) Nature, 438:197.

[18] Zhang YB, Tan YW, Stormer HL, Kim P, (2005) Nature, 438:201.

[19] Heersche HB, Jarillo HP, Oostinga JB, Vandersypen LMK, Morpurgo AF, (2007) Nature, 446:56.

[20] Geim AK, Novoselov KS, (2007) Nat Mater, 6:183.

[21] Wang GX, Shen XP, Yao J, Park J, (2009) Carbon, 47:2049.

[22] Dey AN, (1971) J Electrochem Soc, 118:1547.

[23] Huggins RA, (1999) J Power Sources, 81:13.

[24] Hassoun J, Panero S, Scrosati B, (2009) Fuel Cells, 09:(3)277.

[25] Besenhard JO, (1999) Handbook of Battery Materials, Wiley-VCH.

[26] Li H, Huang XJ, Chen LQ, Wu ZG, Liang Y, (1999) Electrochem Solid-State Lett, 2:547.

[27] Zhou GW, Li H, Sun HP, Yu DP, Wang YQ, Huang XJ, Chen LQ, Zhang Z, (1999) Appl Phys Lett, 75:2447.

[28] Miyaki Y, (2005) U.S. Patent Application, 0181276.

[29] Poizot P, Laruelle S, Grugeon S, Dupont L, Tarascon JM, (2000) Nature, 407:496.

[30] Obrovac MN, Dunlap RA, Sanderson RJ, Dahn JR, (2001) J Electrochem Soc, 148:A576.

[31] Needham SA, Wang GX, Liu HK, (2006) J Power Sources, 159:254.

[32] Oh SW, Bang HJ, Bae YC, Sun YK, (2007) J Power Sources, 173:502.

[33] An LP, Gao XP, Li GR, Yuan TY, Zhu HY, Shen PW, (2008) Electrochimica Acta, 53:4573.

[34] Chen LB, Lu N, Xu CM, Yu HC, Wang TH, (2009) Electrochimica Acta, 54:4198.

[35] Gao XP, Bao JL, Pan GL, Zhu HY, Huang PX, Wu F, Song DY, (2004) J Phys Chem B, 108:5547.

[36] Whittingham MS, (2004) Chem Rev, 104:4271.

[37] Nagaura T, Tozawa K, (1990) Prog Batteries Solar Cells, 9:209.

[38] Ozawa K, (1994) Solid State Ionics, 69:212.

[39] Fong R, Vonsacken U, Dahn JR, (1990) J Electrochem Soc, 137:2009.

[40] Rougier A, Graveau P, Delmas C, (1996) J Electrochem Soc, 143:1168.

[41] Delmas C, Capitaine F, (1996) Abstracts of the 8th International Meeting Lithium Batteries, Electrochemical Society, Pennington, NJ, 8:470.

[42] Chen R, Whittingham MS, (1997) J Electrochem Soc, 144:L64.

[43] Armstrong AR, Bruce PG, (1996) Nature, 381:499.

[44] Padhi AK, Nanjundaswamy KS, Goodenough JB, (1997) J Electrochem Soc, 144:1188.

[45] Yamada A, Chung SC, Hinokuma K, (2001) J Electrochem Soc, 148:A224.

[46] Huang H, Yin SC, Nazar LF, (2001) Electrochem Solid State Lett, 4:A170.

[47] Masquelier C, Wurm C, Morcrette M, Gaubicher J, (2001) International Meeting on Solid State Ionics, Cairns, Australia, The International Society of Solid State Ionics, 2001:A-IN-06.

[48] Chung SY, Bloking JT, Chiang YM, (2002) Nat Mater, 1:123.

[49] Herle PS, Ellis B, Coombs N, Nazar LF, (2004) Nat Mater, 3:147.

[50] Prosini PP, Carewska M, Scaccia S, Wisniewski P, Passerini S, Pasquali M, (2002) J Electrochem Soc, 149:A886.

[51] Wang GX, Ahn JH, Yao J, Bewlay S, Liu HK, (2004) Electrochem Commun, 6:689.

[52] Whittingham MS, (1976) J Electrochem Soc, 123:315.

[53] Cocciantelli JM, Doumerc JP, Pouchard M, Broussely M, Labat J, (1991) J Power Sources, 34:103.

[54] Cocciantelli JM, Menetrier M, Delmas C, Doumerc JP, Pouchard M, Hagenmuller P, (1992) Solid State Ionics, 50:99.

[55] Delmas C, Brethes S, Menetrier M, (1991) J Power Sources, 34:113.

[56] Wakihara M, (1997) The Latest Technology of the New Secondary Battery, CMC, Tokyo, P31.

[57] Broussely M, (1999) J Power Sources, 140:81.

[58] Jansen AN, Kahaian AJ, Kepler KD, Nelson PA, Amine K, Dees DW, Vissers DR, Thackeray MM, (1999) J Power Sources, 902:81.

[59] Zhang X, Ross PN, Kostecki R, Kong F, Sloop S, Kerr JB, Striebel K, Cairns EJ, McLarnon F, (2001) J Electrochem Soc, 148:A463.

[60] Li J, Dahn HM, Krause LJ, Le DB, Dahn JR, (2008) J Electrochem Soc, 155:A812.

[61] Chou SL, Wang JZ, Zhong C, Rahman MM, Liu HK, Dou SX, (2009) Electrochimica Acta, 54:7519.

[62] Needham SA, (2007) PhD Thesis, University of Wollongong.

[63] Lai TL, Shub YY, Huang GL, Lee CC, Wang CB, (2008) J Alloys Compd, 450:318.

[64] Varghese B, Reddy MV, Yanwu Z, Lit CS, Hoong TC, Rao GVS, Chowdari BVR, Wee ATS, Lim CT, Sow CH, (2008) Chem Mater, 20:3360.

[65] Zheng YZ, Zhang ML, (2007) Mater Lett, 61:3967.

[66] Buqa H, Holzapfel M, Krumeich F, Veit C, Novak P, (2006) J Power Sources, 161:617.

[67] Drofenik J, Gaberscek M, Dominko R, Poulsen FW, Mogensen M, Pejovnik S, Jamnik J, (2003) Electrochim Acta, 48:883.

[68] Pejovnik S, Dominko R, Bele M, Gaberscek M, Jamnik J, (2008) J Power Sources, 184:593.

[69] Li J, Dahn HM, Krause LJ, Le DB, Dahna JR, (2008) J Electrochem Soc, 155:A812.

[70] Manickam M, Takata M, (2003) Electrochimica Acta, 48:957.

[71] Lestriez B, Bahri S, Sandu I, Roué L, Guyomard D, (2007) Electrochem Commun, 9:2801.

[72] Guerfi A, Kaneko M, Petitclerc M, Mori M, Zaghib K, (2007) J Power Sources, 163:1047.

[73] Chen L, Xie X, Xie J, Wang K, Yang J, (2006) J Appl Electrochem, 36:1099.

[74] Yuan L, Guo ZP, Konstantinov K, Munroe P, Liu HK, (2006) Electrochem Solid-State Lett, 9:A524.

[75] Ng SH, Wang J, Wexler D, Konstantinov K, Guo ZP, Liu HK, (2006) Angew Chem Int Ed, 45:6896.

[76] Huang XH, Tu JP, Zhang CQ, Xiang JY, (2007) Electrochem Commun, 9:1180.

[77] Huggins RA, (1999) J Power Sources, 81:13.

[78] Grugeon S, Laruelle S, Urbina RH, Dupont L, Poizot P, Tarascon JM, (2001) J Electrochem Soc, 148:(4)A285.

[79] Zhang XJ, Wang GF, Liu XW, Wu HQ, (2008) Mater Chem Phys, 112:726.

[80] Fan J, Wang T, Yu C, Tu B, Jiang Z, Zhao D, (2004) Adv Mater, 16:1432.

[81] Cheng F, Tao Z, Liang J, Chen J, (2008) Chem Mater, 20:667.

[82] Huang XH, Tu JP, Zhang CQ, Chen XT, Yuan YF, Wu HM, (2007) Electrochimica Acta, 52:4177.

[83] Nuli YN, Zhang P. Guo ZP, Wexler D, Liu HK, Yang J, Wang JL, (2009) J Nanosci and Nanotech, 9:(3)1951.

[84] Hang BT, Yoon SH, Okada S, Yamaki J, (2007) J Power Sources, 168:522.

[85] Ju SH, Kang YC, (2009) J Power Sources, 189:185-190.

[86] Lee JH, Paik U, Hackley VA, Choi YM, (2006) J Power Sources, 161:612.

[87] Vuk Uskokovic, (2008) Colloids and Surfaces B: Biointerfaces, 61:250.

[88] Nishide H, Oyaizu K, (2008) Science, 319:737.

[89] Dikin DA, Stankovich S, Zimney EJ, Piner RD, Dommett GHB, Evmenenko G, Nguyen ST, Ruoff RS, (2007) Nature, 448:457.

[90] Chen J, Minett AI, Liu Y, Lynam C, Sherrell P, Wang C, Wallace GG, (2008) Adv Mater, 20:566.

[91] Smith PR, Carey JD, Cox DC, Forrest RD, Silva SRP, (2009) Nanotech, 20:145202.

[92] Morris RS, Dixon BG, Gennett T, Raffaelle R, Heben MJ, (2004) J Power Sources, 138:277.

[93] Chou SL, Wang JZ, Chew SY, Liu HK, Dou SX, (2008) Electrochem Commun, 10:1724.

[94] Pushparaj VL, Shaijumon MM, Kumar A, Murugesan S, Ci L, Vajtai R, Linhardt RJ, Nalamasu O, Ajayan PM, (2007) Proc Natl Acad Sci, 104:(34) 13574.

[95] Wang CY, Li D, Too CO, Wallace GG, (2009) Chem Mater, 21:2604.

[96] Ng SH, Wang JZ, Guo ZP, Chen J, Wang GX, Liu HK, (2005) Electrochimica Acta, 51:23.

[97] Zhang H, Feng C, Zhai Y, Jiang K, Li Q, Fan S, (2009) Adv Mater, 21:2299.

[98] Boukamp BA, Lesh GC, Huggins RA, (1981) J Electrochem Soc, 128:725.

[99] Megahead S, Scrosati B, (1994) J Power Sources, 51:79.

[100] Chan CK, Peng HL, Liu G, McIlwrath K, Zhang XF, Huggins RA, Yi Cui, (2008) Nature Nanotech, 3:(1)31.

[101] Kasavajjula U, Wang CS, Appleby AJ, (2007) J Power Sources, 163:1003.

[102] Wilson AM, Dahn JR, (1995) J Electrochem Soc, 142:326.

[103] Wilson AM, Reimers JN, Fuller EW, Dahn JR, (1994) Solid State Ionics, 74:249.

[104] Holzapfel M, Buqa H, Scheifele W, Novak P, Petrat FM, (2005) Chem Commun, 1566.

[105] Hummers W, Offeman RJ, (1958) Am Chem Soc, 80:1339.

[106] Kovtyukhova NI, Ollivier PJ, Martin BR, Mallouk TE, Chizhik SA, Buzaneva EV, Gorchinskiy AD, (1999) Chem Mater, 11:771.

[107] Chew SY, Guo ZP, Wang JZ, Chen J, Munroe P, Ng SH, Zhao L, Liu HK, (2007) Electrochem Commun, 9:1877.

[108] Tang LH, Wang Y, Li YM, Feng HB, Lu J, Li JH, (2009) Adv Funct Mater, 19:2782.

[109] Xie J, Cao GS, Zhao XB, (2004) Mater Chem and Phys, 88:295.

[110] Fang M, Wang KG, Lu HB, Yang YL, Nutt S, (2009) J Mater Chem, 19:7098.

[111] Chou SL, Wang JZ, Choucair M, Liu HK, Stride JA, Dou SX, (2010) Electrochem. Commun. 12:303.

[112] Zhang T, Gao J, Zhang HP, Yang LC, Wu YP, Wu HQ, (2007) Electrochem. Commun. 9:886.

[113] Paek S, Yoo E, Honma I, (2009) Nano Lett. 9:72.

[114] Zhang T, Gao J, Fu LJ, Yang LC, Wu YP, Wu HQ, (2007) J. Mater. Chem. 17:1321.

[115] Graetz J, Ahn CC, Yazami R, Fultz B, (2003) Electrochem. Solid-State Lett. 6:A194.

[116] Kijima N, Ikeda T, Oikawa K, Izumi F, Yoshimura Y, (2004) J Solid State Chem, 177:1258.

[117] Jiao F, Bruce PG, (2007) Adv Mater, 19:657.

[118] Sugantha M, Ramakrishnan PA, Hermann AM, Warmsingh CP, Ginley DS, (2003) Int J Hydrogen Energy, 28:597.

[119] Reddy AL, Shaijumon MM, Gowda SR, Ajayan PM, (2009) Nano Lett, 9(3):1002.

[120] Kunduraci M, Amatucci GG, (2006) J Electrochem Soc, 153(7):1345.

[121] Wang HE, Lu Z, Qian D, Fang S, Zhang J, (2008) J Alloy Compd, 466:250.

[122] Subramanian V, Zhu HW, Vajtai R, Ajayan PM, Wei BQ, (2005) J Phys Chem B, 109:20207.

[123] Du GH, Yuan ZY, Tendeloo GV, (2005) Appl Phys Lett, 86:063113.

[124] Wang X, Li Y, (2002) Chem Commun, 7:764.

[125] Wang JZ, Chou SL, Chew SY, Sun JZ, Forsyth M, MacFarlane DR, Liu HK, (2008) Solid State Ionics, 179:2379.

[126] Ellis B, Kan WH, Makahnouk WRM, Nazar LF, (2007) J Mater Chem, 17:3248.

[127] Meng Z, Peng Y, Yu W, Qian Y, (2002) Mater Chem Phys, 74:230.

[128] Luo JY, Zhang JJ, Xia YY, (2006) Chem Mater, 18:5618.

LIST OF PUBLICATIONS

(1) **Zhong C**, Wang JZ, Chou SL, Konstantinov K, Rahman MM, Liu HK, "Nanocrystalline NiO hollow spheres in conjunction with CMC for lithium-ion batteries", (2010) *Journal of Applied Electrochemistry*, 40:1415-1419.

(2) **Zhong C**, Wang JZ, Zhu ZZ, Chou SL, Chen ZX, Li Y, Liu HK, "Hydrothermal synthesis of nanostructured MnO_2 under magnetic field for rechargeable lithium batteries", (2010) *Journal of Solid State Electrochemistry*, 14:1743-1747.

(3) Wang JZ, **Zhong C**, Chou SL, Liu HK, "Flexible Free-standing Graphene-silicon Composite Film for Lithium-ion Batteries", (2010) *Electrochemistry Communications*, doi:10.1016/j.elecom.2010.08.008.

(4) Du GD, **Zhong C**, Zhang P, Guo ZP, Chen ZX, Liu HK, "Tin dioxide/carbon nanotubes composites with high uniform SnO_2 loading as anode materials for lithium ion batteries", (2010) *Electrochimica Acta*, 55:2582-2586.

(5) Chou SL, Wang JZ, **Zhong C**, Rahmana MM, Liu HK, Dou SX, "A facile route to carbon-coated SnO_2 nanoparticles combined with a new binder for enhanced cyclability of Li-ion rechargeable batteries", (2009) *Electrochimica Acta*, 54:7519-7524.

(6) Rahman MM, Chou SL, **Zhong C**, Wang JZ, Wexler D, Liu HK, "Spray pyrolyzed NiO-C nanocomposite as an anode material for the lithium-ion battery with enhanced capacity retention", (2010) *Solid State Ionics*, 180:1646-1651.

(7) Wang JZ, Chou SL, Liu H, Wang GX, **Zhong C**, Chew SY, Liu HK, "Highly flexible and bendable free-standing thin film polymer for battery application", (2009) *Materials Letters*, 63:2352-2354.